

Article

Commissioning of a High Pressure Time Projection Chamber with Optical Readout

A. Deisting ⁸ * , A. V. Waldron ³ * , E. Atkin ³ , G. J. Barker ¹¹, A. Basharina-Freshville ¹⁰, C. Betancourt ¹², S. B. Boyd ¹¹, D. Brailsford ⁵ , Z. Chen-Wishart ⁸, L. Cremonesi ^{10,α} , A. Dias ⁸ , P. Dunne ³ , J. Haigh ¹¹, P. Hamacher-Baumann ⁹ , S.B. Jones ¹⁰ , A. Kaboth ⁸, A. Korzenev ², W. Ma ⁹, P. Mermod ² †, M. Mironova ^{3,6}, J. Monroe ⁸ , R. Nichol ¹⁰, T.S. Nonnenmacher ³, J. Nowak ⁵ , W. Parker ^{8,β}, H. Ritchie-Yates ⁸, S. Roth ⁹, R. Saakyan ¹⁰, N. Serra ¹², Y. Shitov ^{3,4}, J. Steinmann ⁹, A. Tarrant ^{8,γ} , M. A. Uchida ^{3,1}, S. Valder ¹¹, M. Ward ^{8,7}, M. Wascko ³ 

¹ Cavendish Laboratory, Cambridge CB3 0HE, UK; m.a.uchida@imperial.ac.uk

² DPNC Université de Genève, 1205 Genf, Switzerland; korzenev@mail.cern.ch (A.K.); Philippe.Mermod@cern.ch (P.M.);

³ The Blackett Laboratory, Imperial College London, London SW7 2BW, UK; e.atkin17@imperial.ac.uk (E.A.); p.dunne12@imperial.ac.uk (P.D.); maria.mironova@physics.ox.ac.uk (M.M.); toby.nonnenmacher14@imperial.ac.uk (T.N.); Shitov@JINR.ru (Y.S.); m.wascko@imperial.ac.uk (M.W.)

⁴ JINR, 141980 Dubna, Russia

⁵ Lancaster University, Bailrigg, Lancaster LA1 4YW, UK; d.brailsford@lancaster.ac.uk (D.B.); j.nowak@lancaster.ac.uk (J.N.)

⁶ Department of Physics, Oxford University, Oxford OX1 3PU, UK

⁷ Queen's University, Kingston, ON K7L 3N6, Canada; mark.ward@snolab.ca

⁸ Royal Holloway, University of London, Egham Hill, Egham, TW20 0EX, UK; Zachary.Chen-Wishart.2016@live.rhul.ac.uk (Z.C.-W.); Adriana.Dias.2011@live.rhul.ac.uk (A.D.); Asher.Kaboth@rhul.ac.uk (A.K.); jocelyn.monroe@rhul.ac.uk (J.M.); william.parker@physics.ox.ac.uk (W.P.); Harrison.Ritchie-Yates.2013@live.rhul.ac.uk (H.R.-Y.); A.Tarrant@liverpool.ac.uk (A.T.)

⁹ III. Physikalisches Institut, RWTH Aachen University, 52056 Aachen, Germany; hamacher.baumann@physik.rwth-aachen.de (P.H.-B.); ma@physik.rwth-aachen.de (W.M.); stefan.roth@physik.rwth-aachen.de (S.R.); jochen.steinmann@physik.rwth-aachen.de (J.S.)

¹⁰ University College London, Gower St, Kings Cross, London WC1E 6BT, UK; anastasia.freshville@ucl.ac.uk (A.B.-F.); l.cremonesi@qmul.ac.uk (L.C.); sebastian.jones.17@ucl.ac.uk (S.B.J.); r.nichol@ucl.ac.uk (R.N.); r.saakyan@ucl.ac.uk (R.S.)

¹¹ University of Warwick, Coventry CV4 7AL, UK; g.j.barker@warwick.ac.uk (G.J.B.); S.B.Boyd@warwick.ac.uk (S.B.B.); J.Haigh.2@warwick.ac.uk (J.H.); s.valder@warwick.ac.uk (S.V.)

¹² Physik-Institut, Universität Züriche, Rämistrasse 71, 8006 Zürich, Switzerland; christopher.betancourt@cern.ch (C.B.); nicola.serra@cern.ch (N.S.)

* Correspondence: alexander.deisting@cern.ch (A.D.), a.waldron@imperial.ac.uk (A.V.W.)

^α Now at: Queen Mary University of London, Mile End Road, London E1 4NS, UK

^β Now at: University of Oxford, Clarendon Laboratory, Parks Road, Oxford OX1 3PU, UK

^γ Now at: University of Liverpool, The Oliver Lodge Laboratory, Liverpool L69 7ZE, UK

† Passed away on 20 August 2020

Version 21st May 2021 submitted to *Instruments*

Keywords: Time Projection Chamber; Optical Readout; Neutrino Detector Development; Hybrid Charge and Optical Readout; Gaseous Detectors

Measurements of proton-nucleus scattering and high resolution neutrino-nucleus interaction imaging are key to reduce neutrino oscillation systematic uncertainties in future experiments. A High Pressure Time Projection Chamber (HPTPC) prototype has been constructed and operated at Royal Holloway University of London and CERN as a first step in the development of a HPTPC capable of performing these measurements as part of a future long-baseline neutrino oscillation experiment such

8 as the Deep Underground Neutrino Experiment. In this paper we describe the design and operation of
9 the prototype HPTPC with an argon based gas mixture. We report on the successful hybrid charge and
10 optical readout, using four CCD cameras, of signals from ^{241}Am sources.

11 1. Introduction

12 High Pressure Time Projection Chambers (HPTPCs) are an area of growing international interest.
13 The Deep Underground Neutrino Experiment (DUNE) envisions the use of an HPTPC as part of its
14 near detector and European groups have held a series of workshops on HPTPC development over
15 the last five years. Given the recent indication of non-zero CP violation in the Tokai to Kamioka (T2K)
16 experiment's data [1], it is timely to quantify the potential impact of HPTPC neutrino (ν) detector
17 technology on mitigation of the dominant neutrino-interaction cross-section uncertainties for the future
18 long-baseline neutrino oscillation programme.

19 Final State Interactions (FSIs) of nucleons produced in neutrino interactions are among the leading
20 sources of systematic uncertainties in neutrino oscillation experiments [2]. Gas TPCs are ideal for
21 precisely characterizing FSI effects because of their high track reconstruction efficiency, low momentum
22 threshold and 4π angular coverage of final state particles, which are all key to distinguishing between
23 interaction models. For example, the proton multiplicity and momentum distributions for neutrino
24 charged current interactions on argon calculated by the neutrino interaction Monte Carlo generators
25 NEUT [3] and GENIE [4] are highly discrepant in the fraction of events with few ejected protons, and
26 at low proton momentum, below $250\text{ MeV}/c$ [5]. This is below the proton detection threshold in water
27 Cherenkov detectors ($1100\text{ MeV}/c$) and below that of liquid argon TPCs, around $400\text{ MeV}/c$ [6]. A
28 gas-filled HPTPC however has a low enough momentum threshold to resolve FSI model discrepancies,
29 and therefore an HPTPC has unique capability to address the dominant systematic uncertainty in
30 neutrino oscillation measurements.

31 This paper describes the design, commissioning and calibration of a prototype HPTPC detector.
32 Section 1.1 describes the prototype detector and readout design, Sec. 2 motivates the choice of gas
33 target, Sec. 3 describes the high pressure vessel and the gas system, Sec. 4 details the TPC hardware
34 including its high voltage supply and data acquisition system. In Sec. 5 and Sec. 6 the analysis of camera
35 images and charge signal waveforms, respectively, are explained and results of the commissioning
36 measurements are presented. Section 7 contains a combined analysis of the optical and charge readout
37 signals.

38 1.1. Design considerations

39 The need for lower momentum measurements [5] motivates the choice of a gas-filled detector
40 for the task of measuring neutrino-nucleus scattering. Another key consideration for the detector is
41 that it has sufficient target mass to achieve a low statistical error on measured final state kinematic
42 distributions. This requirement drives the choice of a high pressure gas as it has higher density and
43 therefore higher mass.

44 The momentum threshold goal for our HPTPC prototype is designed to probe the discrepant
45 low-momentum region of parameter space [5]. The threshold goal for a well-reconstructed proton in
46 argon at 5 barA (10 barA) is $\sim 50\text{ MeV}/c$ (about $70\text{ MeV}/c$). This drives choices in the readout design,
47 such that at $\sim 50\text{ MeV}/c$ a proton track is sampled by ~ 10 measurements in the readout plane. We also
48 aim to cover the momentum range above $320\text{ MeV}/c$ (50 MeV kinetic energy) where no measurements
49 currently exist [5].

50 The track length of a $50\text{ MeV}/c$ proton in a 5 barA argon target is $\sim 10\text{ mm}$. To achieve 10 samples
51 along such a track, a readout plane with a granularity of order 1 mm^2 is needed. Conventional
52 segmented pad planes of current experiments (e.g. T2K) have a pad size of order 1 cm^2 at a cost of
53 about 8 EUR per channel. Given that an area of 20 m^2 is realistic for the readout plane of a future
54 HPTPC near detector at a long-baseline neutrino oscillation experiment, a solution with a lower cost
55 per channel is attractive.

The transverse diffusion in pure Ar at 5 barA is too large to allow for drift lengths of several 10 cm whilst permitting 1 mm track sampling. When adding a quencher such as CO₂ to the argon gas, the diffusion is reduced, allowing for 1 mm track sampling and a 50 cm drift length (Sec. 2).

1.2. Optical readout

A relatively new development in TPC readout technology that offers a low cost per channel is optical readout. TPCs have been in use since the late 1970s, typically with direct readout of the drifted charge. CCD optical readout of time projection chambers was first demonstrated in ~1990 by [7], [8] and [9], and more recently has been developed by the DMTPC project for direction-sensitive dark matter searches [10], by the CYGNO collaboration [11], by the O-TPC [12] detector for precision nuclear physics cross section measurements, for X-ray imaging [13], for proton imaging [14] and by the CERN gas detectors group for gamma detection [15]. DMTPC demonstrated that a TPC with optical readout can realise a sub-mm² segmentation over a readout plane with an area larger than 1 m² [16]. For a recent review, we refer the reader to [17].

An optical TPC is instrumented with a cathode and (several) anode electrodes which define its signal collection and amplification regions. Ionisation electrons from charged particles propagating through the TPC move in the drift field to the amplification region where avalanche charge multiplication and scintillation photon production occurs (Fig. 1a). A schematic of how our optical TPC operates is shown in Fig. 1. The anodes may also be equipped with charge readout to provide high resolution tracking in the drift direction, as in [16]. CCD or CMOS cameras view the amplification plane through lenses from outside of the pressure vessel containing the TPC and target gas, collecting the scintillation light and subsequently providing tracking information in the amplification plane. The design considerations for optical TPCs are described in detail in [17].

In an optical TPC, the track reconstruction resolution in the amplification plane depends on the optical plate scale. This scale is determined by the requirement that the object be in focus, which sets a minimum object distance given an image distance and focal length of the lens, and on the optical system demagnification, which is the ratio of the object to image distances. Typical demagnification values are 5-10. The area of the amplification region imaged by each CCD pixel (a 'vixel'), determines the smallest unit of track segment measurement possible with a given optical system and detector geometry. We define a vixel to be a box with an area of A_{vixel} for the sides parallel to the readout plane and a height corresponding to the length an electron drifts during one CCD exposure time.

The minimum sensible vixel size is determined by the transverse diffusion of the ionization electrons from a particle track in the TPC, as they drift to the amplification region. The track reconstruction resolution in the drift direction is determined by the number of samples along the track, which depends on the track length, drift velocity, and readout rate.

The momentum threshold for track reconstruction depends on the minimum deposited energy at which a cluster of vixels can be identified as a track. This depends primarily on the signal-to-noise ($\mathcal{S} : \mathcal{N}$) ratio per vixel. In general, vixels with $\mathcal{S} : \mathcal{N} > 5$ can be identified as part of a particle track [18].

The expected signal size, that is the number of photons collected per pixel, is given by

$$N_{\mathcal{S}} = \left[\frac{\varepsilon_{\text{particle}}}{W} \times G \times (\gamma/e^-) \right] \times \left[T_{\text{anode}} \times T_{\text{cathode}} \times T_{\text{window}} \times T_{\text{lens}} \right] \times \left[\frac{1}{16 \times f_{\text{stop}}^2 \times (1 + m_d)^2} \right] \times QE^* \quad (1)$$

where the first term in brackets is the number of photons produced in the amplification region, which depends on the ionization energy deposited per vixel by a particle with energy $\varepsilon_{\text{particle}}$, the energy to liberate one electron-ion pair in the gas W , the gas amplification factor (gain) G , and the scintillation photon-to-electron ratio (γ/e^-) of the gas. The second term in brackets is the total photon transmission of the system, which depends on the transmittance of the lens (T_{lens}), the pressure vessel window

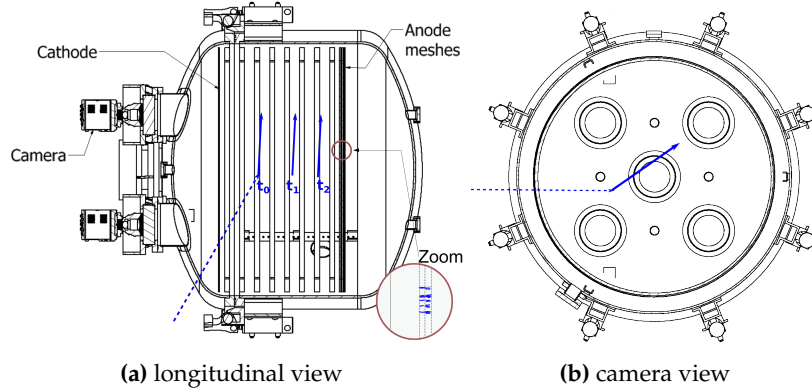


Figure 1. Cross-sectional view of the HPTPC through the (a) plane parallel to the drift field E and (b) the plane perpendicular to E . A particle (dotted line) scatters on an atom or molecule in the gas at the time t_0 , ejects a charged particle from the nucleus which in turn ionises gas atoms along its trajectory (arrow, Fig. (a)). These ionisation electrons are moved by E towards the anode meshes and are eventually amplified. The positions of these ionisation electrons as they drift are labelled t_1 and t_2 . Photons produced during the amplification are then imaged by cameras and provide the 2D projection of the interaction (Fig. (b)), the zoomed inlet in (a) illustrates where avalanches form and the photons are emitted.

99 (T_{window}), and the cathode (T_{cathode}) and anode meshes (T_{anode}) through which the CCD views the
 100 amplification region, averaged over the scintillation emission spectrum. The third term in brackets is
 101 the geometric acceptance of the optical system, which depends on the lens aperture to focal length
 102 ratio (f_{stop}) and the demagnification (m_d). The last term QE^* is the CCD quantum efficiency averaged
 103 over the scintillation emission spectrum. Other elements which enhance (e.g. reflections) or reduce the
 104 signal are not taken into account.

105 The noise per vixel depends on the quadrature sum of the shot noise which is $\sqrt{N_{\text{signal}}}$, the read noise
 106 N_{read} , and the dark rate of the camera times the exposure time ($N_{\text{pixels}} \cdot R(T) \cdot t_{\text{exposure}}$):

$$N_{\mathcal{N}} = \sqrt{N_{\text{signal}} + N_{\text{read}}^2 + N_{\text{pixels}} \cdot R(T) \cdot t_{\text{exposure}}} \quad (2)$$

107 In the dark noise term, N_{pixels} is the number of CCD pixels grouped into a readout bin, t_{exposure} is
 108 the exposure time of a pixel, and $R(T)$ is the dark rate which is a function of temperature T . Here,
 109 a readout bin is a group of camera pixels which is grouped together and read out as one. Typically
 110 a cooled CCD can suppress the dark current to < 0.1 electrons/pixel/s, whilst the read noise is of
 111 order 10 electrons RMS, so for exposure times of order seconds the read noise dominates. The area
 112 determined by $N_{\text{pixels}} \times A_{\text{vixel}}$ can be thought of as an effective pad size of the readout, where A_{vixel} is
 113 the vixel area imaged by one CCD pixel.

114 In the prototype detector described here, the vixel size is $\sim 236 \times 236 \mu\text{m}^2$ in the readout plane, and the
 115 readout binning operated was 4×4 ($N_{\text{pixels}} = 16$) and 8×8 ($N_{\text{pixels}} = 64$), producing an effective pad
 116 size after readout binning of $\sim 0.86 \text{ mm}^2$ and $\sim 3.46 \text{ mm}^2$ respectively. In this way, a 10 mm long track,
 117 corresponding to a 50 MeV/c proton, is sampled at 5-10 points, as the vixel area in the readout plane is
 118 a square. The area A_{vixel} is calculated by dividing the area imaged by one camera ($\sim 71 \times 71 \text{ cm}^2$) by
 119 the camera's pixel layout of $3056 \times 3056 \text{ pixel}^2$ and accounting for the readout binning. The height of a
 120 vixel corresponds to the full drift length, since we operated the cameras with an exposure times of 0.5
 121 to 1 s.

122 1.3. HPTPC prototype overview

123 The prototype HPTPC detector described here is housed in a stainless steel (type 304L) vessel
124 (Sec. 3) of volume 1472 L which is rated to 5 barG. We use barA to denote absolute pressure and barG
125 for pressure measurements relative to ambient pressure. The vessel features feed-throughs for high
126 voltage and instrumentation, optical windows and camera mounting hardware. The detector layout is
127 sketched in Fig. 1. The vessel's internal rail system supports a TPC, which has 44.7 cm drift length and
128 111 cm diameter (Sec. 4). The TPC drift region is enclosed by the cathode mesh at negative voltage and
129 the first anode mesh. Two more anode meshes at increasing positive voltage follow in order to amplify
130 primary ionisations.

131 The working principle of the detector is illustrated in Fig. 1. A particle entering the drift volume
132 (*e.g.* a neutrino) scatters at a time t_0 on an atom or molecule, thereby ejecting protons from the
133 struck nucleus. These final state particles ionise gas atoms and molecules along their path (indicated
134 schematically with an arrow in Fig. 1a). The resulting primary ionisation electrons drift in the electric
135 field E towards the anode meshes and are eventually amplified in the high electric field close to the
136 meshes' wires and between the meshes. In the avalanche, electrons and photons are produced and the
137 latter can then be recorded by the cameras, which provide an image of the interaction (Fig. 1b) with
138 the locations as well as the intensity, where the latter is proportional to the energy deposited in the
139 drift volume. Reading out the charge signals induced by the avalanches at the anode meshes provides
140 additional time information. The duration of these charge signals in the anodes will be proportional to
141 the track length projected into the drift direction. The advantages of using this charge readout include
142 the ability to calibrate gas mixtures that emit very little light and the ability to correlate light and
143 charge signals.

144 The optical readout system for the HPTPC prototype described here uses four CCD cameras,
145 which are mounted onto the high pressure vessel and image the amplification stage from the
146 cathode side, through the windows of the pressure vessel, as well as through the cathode and anode
147 meshes. Each camera views one quadrant of the amplification region, through lenses focussed on the
148 amplification plane (Sec. 4.6). The HPTPC's charge readout system reads the charge induced on the
149 whole (un-segmented) plane of each of the three anodes. The signals are decoupled, amplified and
150 shaped by commercial front end electronics, and subsequently digitized synchronously in time with
151 the CCD data acquisition.

152 Throughout the paper we use a Cartesian coordinate system in which all electrodes are x/y planes
153 at a constant z and where the z axis is parallel to the electric field direction. The origin is located in the
154 centre of the anode 1 mesh and z increases towards the cathode. In the x/y planes we occasionally use
155 polar coordinates where r points from the centre to the edge of the TPC.

156 2. Gas Requirements

157 The typical wavelength sensitivity range of CCD cameras is 350 nm to 850 nm (Sec. 4.6), and
158 therefore the gas is required to have a high photon (or electro-luminescence) yield in this wavelength
159 range. A noble gas is the obvious choice for the dominant part of the gas mixture, since it lacks the
160 rotational and vibrational degrees of freedom which absorb photons.

161 Gaseous argon has been shown to emit not only light in the Vacuum Ultra Violet (VUV), but also in the
162 near infra-red (NIR) wavelengths [19]. Scintillation light measurements at pressures higher than 1 barA
163 show that the NIR light yield normalised to the number of amplification electrons decreases with
164 increasing pressure [20]. This can, however, be compensated by a larger gain of the amplification stage.
165 In [20] the authors show that additions of CF_4 leads to a high photon yield in the visible (VIS) and NIR:
166 In Ar gas with a small (5 %) admixture of CF_4 , the scintillation photon yield in optical wavelengths is
167 0.1-0.3 per avalanche electron, and is a weak function of the reduced electric field. Neon, on the other
168 hand, emits in the NIR region as well [21]. Admixtures of nitrogen have been shown to result in a
169 higher intensity electro-luminescence in the VIS, as compared to the NIR neon electro-luminescence. A
170 Ne/ N_2 mixture is therefore also a good candidate for a TPC with optical readout.

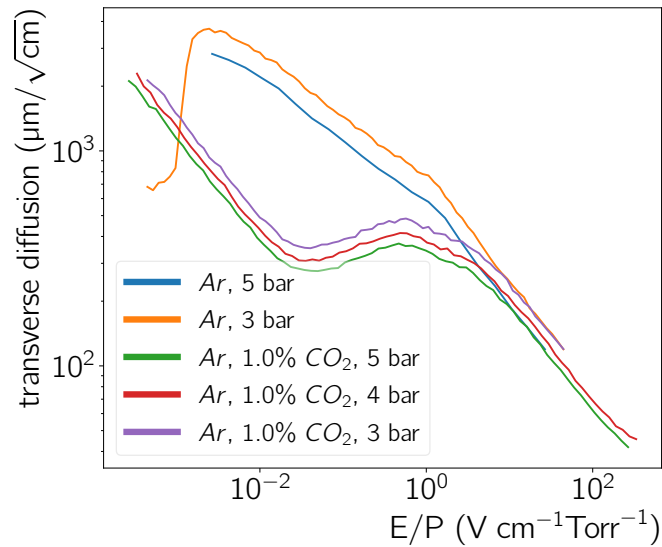


Figure 2. Transverse diffusion for pure argon and different Ar/CO₂ mixtures simulated using MAGBOLTZ [23].

171 We chose argon as the principle component of our gas mixture because an Ar based mixture is foreseen
 172 for the HPTPC of DUNE's near detector. Demonstrating the technological readiness of an HPTPC
 173 with this gas mixture makes a strong case for using this technology as part of a near detector in a
 174 long-baseline neutrino oscillation experiment with far detectors with identical targets. Argon has
 175 already been proven to emit light at high pressure in the wavelength range to which our cameras are
 176 sensitive [22]. Furthermore argon is considerably less expensive than neon gas.

177 Operating a TPC with pure argon comes with the disadvantage that stable operation is notoriously
 178 difficult at high gains, and that the transverse diffusion is high. For a drift field of $\sim 200 \text{ V cm}^{-1}$ the
 179 transverse diffusion in pure Ar at 5 barA ($E/P \sim 0.05 \text{ V/cm/Torr}$) is about $1000 \mu\text{m}/\sqrt{\text{cm}}$ [23] as can
 180 be seen in Fig. 2. An optical readout with cameras provides an effective segmentation of the readout
 181 plane into segments of less than a 1 mm^2 , as discussed in Sec. 1.1. The diffusion in pure argon for
 182 drift lengths of several 10s of cm is too large to exploit the advantages of a fine segmentation. Adding
 183 a quencher reduces the diffusion and enables higher gains under more stable operating conditions.
 184 For example, in Ar/CO₂ (99/1) the diffusion is reduced by an order of magnitude as compared to
 185 pure argon (Fig. 2). This allows drift lengths of up to 50 cm whilst retaining the requirement that the
 186 transverse diffusion not exceed twice the readout segment length of 1 mm.

187 The typical quencher for an Ar mixture is carbon-dioxide, however CO₂ has been shown to lower
 188 the light yield [22]. N₂ on the other hand is not a good quencher in Ar, but provides small reduction
 189 in the light yield [22]. In this paper we experimented with pure Ar and different Ar/CO₂, Ar/N₂
 190 and Ar/CO₂/N₂ mixtures to establish which gas provides the largest light gain in the NIR (Sec. 5.4).
 191 During the operation of the high pressure TPC periods of sparking occurred (Sec. 5.1), which had a
 192 large influence on the gas eventually used in the measurements presented in this paper. Other gases
 193 and admixtures are also interesting to study, however, these studies are not part of the measurements
 194 for this paper.

195 3. High pressure vessel design

196 The pressure vessel design is shown in Fig. 3. The vessel is 304L stainless steel, with an inner
 197 (outer) diameter of 140 cm (142 cm). The total length of the vessel, including the domed ends, is
 198 138.6 cm; the length of the domed sections is 32.5 cm each, leaving a length of 73.6 cm in the cylindrical
 199 straight section which hosts the TPC. The weight of the vessel (empty) is 2370 kg.

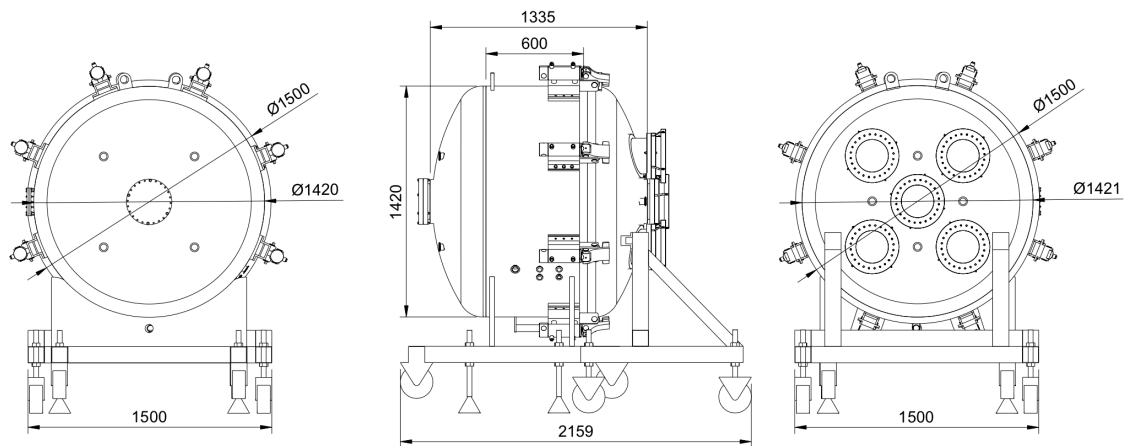


Figure 3. Schematic drawings of the pressure vessel: end view of the back side (left), side view with the vessel door to the left (middle), and end view of the door side (right).

200 One of the domed ends of the cylinder is fully detachable to gain access to the vessel's interior, *e.g.*
 201 for the TPC installation. The detachable door is connected to the body of the vessel via a large DN 1500
 202 flange. The door and the body of the vessel are mounted to separate steel frames with wheels, both
 203 with adjustable feet for elevation adjustment. A double O-ring seal of viton and a rectangular silicone
 204 layer between the door and body flange sides provide gas tightness. The door and body flanges are
 205 clamped together with 8 hydraulic pistons and 8 screwable clamps, with a force up to 50 N m. The
 206 helium leak tightness specification is 2.5×10^{-9} mbar L s⁻¹.

207 The vessel flanging is indicated in Fig. 3. The door is equipped with five DN200 and four KF40
 208 flanges (Fig. 3, left), while the body features one DN200 and four KF40 flanges on the side opposite
 209 of the door (Fig. 3, right), four KF25 flanges and one KF40 flange on the left side of the body (Fig. 3,
 210 middle), and four KF40 flanges on the right side. The KF25 and KF40 flanges are used for High Voltage
 211 (HV), gas and vacuum system feed-throughs. The 5 DN200 flanges on the door are each equipped
 212 with a custom optical window flange and camera mount incorporating a 60 mm thick quartz optical
 213 window. The body flanges host two independent pressure relief systems. The first is a 5 barG burst
 214 disk backed by a 5 barG pressure relief valve. The second, on an independent body flange, is a 6 barG
 215 burst disk.

216 The interior of the vessel houses three steel rails that run longitudinally along the walls, separated
 217 at approximately 120°, to allow mounting of equipment inside the chamber. The interior surfaces are
 218 shot blasted.

219 The vessel is rated to a 6 barA. To verify this after construction the vessel was filled with water and
 220 subjected to the test pressure of 7.2 barG for 10 minutes. No evidence of leaks or material deformation
 221 was observed. The hydrostatic pressure was subsequently decreased to the working pressure of 5 bar
 222 absolute pressure and maintained for 90 minutes to verify the tightness of the pressurized vessel. After
 223 the test the vessel was emptied and dried with nitrogen gas. All optical windows were installed during
 224 this test, validating the design of the custom DN200 optical flanges. Given the 1472 L volume, the
 225 vessel is a category IV pressure vessel. This hydrostatic test was used to follow conformity assessment
 226 procedure MAT-17-CE-G-CRTO02/17 to obtain the declaration of conformity with pressure vessel
 227 directive 97/23/CE.

228 3.1. Gas system

229 The gas and evacuation system for the HPTPC prototype detector described here is shown in
 230 Fig. 4.

231 The gas filling strategy for the HPTPC foresees to evacuate (and purge) the vessel prior to the
 232 target gas fill. An Agilent Triscroll 800 dry vacuum pump is used to pump down the vessel to a

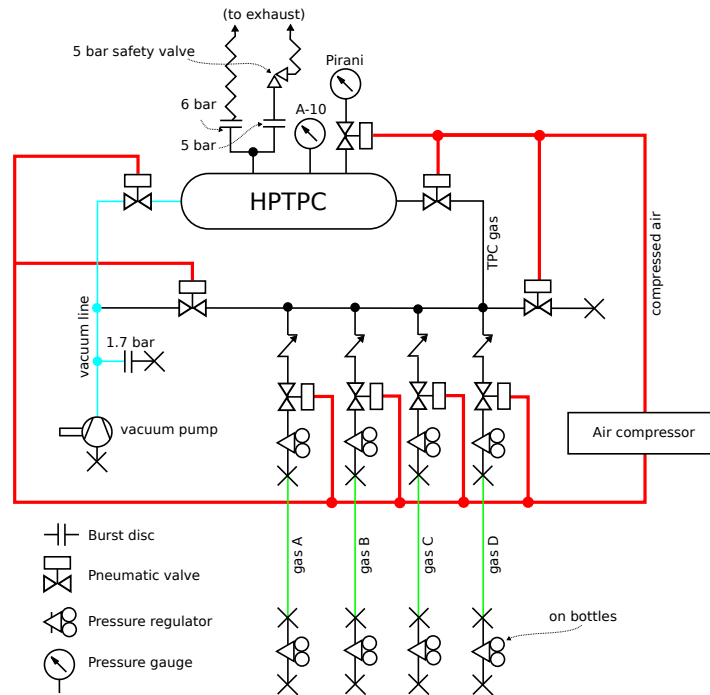


Figure 4. Diagram of the gas fill and evacuation system for the HPTPC vessel.

233 pressure of approximately 1×10^{-6} barA before gas operations. The same pump is used to evacuate
 234 the fill line from the gas system to the vessel to reduce contamination, during the filling procedure or in
 235 case a gas fill is topped up to a higher pressure. The system enables mixing of gases from four different
 236 inputs, using eight Aura gas pressure regulators with manometers and threaded connections (four in the
 237 primary 200 – 10 bar stage and four in the secondary 10 – 0 bar stage). Mixtures are achieved by
 238 filling with different gases in turn, while the respective proportions are adjusted by partial pressure.
 239 The lines from gas bottle to the gas system are purged using gas from the bottle whenever a new bottle
 240 is connected.

241 All valves can be opened and closed remotely using the slow control system. The system consists
 242 of eight 0.5 in Swagelok solenoid valves and one 1.5 in Carten solenoid valve, all pneumatically
 243 activated. The gas pressure is monitored by a Wika A-10 digital pressure gauge (from 0.8 barA to
 244 6 barA absolute pressure), and by an Inficon PGC550 combined capacitance-Pirani vacuum gauge
 245 for pressures between 5×10^{-8} barA to just below atmospheric pressure. Since the Pirani gauge is
 246 not suitable for over-pressure it is protected by an electronically controlled valve when the pressure
 247 exceeds 0.8 barA. The slow control system logs the gas pressure from the two gauges as well as the
 248 ambient laboratory temperature, measured with sensor SynAccess TS-0300, for later use in the analysis.

249 4. Time Projection Chamber

250 The principal components of the time projection chamber are the field cage and the electrodes
 251 that define the drift and amplification regions. Figure 5 shows the field cage ring structure,
 252 and amplification region before the assembly is inserted into the pressure vessel (left), and
 253 *in-situ*—including the cathode—before the pressure vessel is closed (right).

254 4.1. Field cage

255 The field cage (Fig. 5a) is constructed of 12 copper rings with an inner diameter of 111 cm, and
 256 length of 1.0 cm in z and 0.6 cm in r . The distance between two neighbouring rings is 2.5 cm. Each
 257 ring is supplied with HV via the cathode in series with 3 M Ω resistors held in place with compression
 258 fittings between subsequent rings. The last ring on the field cage facing the amplification region is

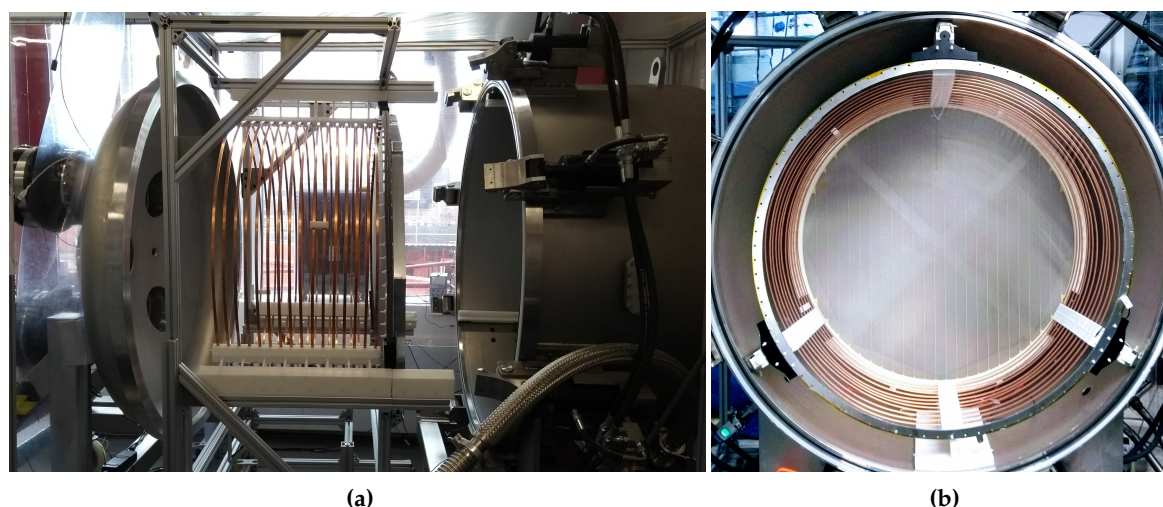


Figure 5. (a) The field cage before insertion into the pressure vessel and (b) after insertion. The latter picture is photographed through the high-transparency cathode towards the amplification region and shows the full TPC.

259 connected to ground via a resistor whose value is chosen depending on the spacing between the final
 260 ring and the amplification region to maintain field uniformity. The total length of the field cage is
 261 42.4 cm, resulting in a 44.7 cm drift distance between the cathode and the amplification region.

262 The field cage assembly is supported from the three internal rails on the pressure vessel by
 263 machined Delrin parts. One set of these supports houses the resistor chain. The size of the support
 264 between the vessel rails and the field cage is adjustable.

265 4.2. Cathode electrode

266 The cathode electrode is a 25 lpi (lines per inch) steel mesh made from 27 μm diameter wires. Due
 267 to its low wire density the mesh has a calculated transparency of $\sim 97\%$, which allows for camera
 268 imaging of the amplification region through the cathode mesh (Fig. 5b).

269 A 122 cm \times 122 cm square of this mesh was stretched to a tension of 6.4 N cm^{-1} on a Grünig
 270 G-STRETCH 210 mesh stretching machine. After stretching, the mesh was epoxied using DP460
 271 epoxy to a circular stainless steel ring, with 118 cm outer diameter, 112 cm inner diameter, and 0.3 cm
 272 thickness.

273 The tension measurement employs a Teren Instruments HT-6510N tension meter; measurements
 274 are made at 9 points on the mesh. The average tension reported here is the average of measurements at
 275 these 9 locations, after the stretching and relaxation procedure is completed. The standard deviation of
 276 repeated tension measurements across the 9 spatial locations is measured to be $0.4 - 0.8 \text{ N cm}^{-1}$ [24].

277 The cathode assembly is supported on the three internal rails of the vessel with machined Delrin
 278 pieces. The spacing of the cathode to the first field cage ring is constrained by the Delrin supports of
 279 the cathode and the mating support parts of the closest field cage ring.

280 4.3. Gas amplification stage

281 The amplification stage is constructed from three electrodes (anodes), separated by two resistive
 282 spacers. The resistive spacers are 121 cm outer diameter, 112 cm inner diameter rings, with 24 wide
 283 beams, 0.1 cm each, crossing them, laser cut from polyester shim stock. The spacer beams are visible as
 284 the vertical lines in the anode plane in Fig. 5b.

285 The amplification region flatness is constrained by its support frame, which consists of two ring-shaped
 286 frames made of Nylon bolted together, which sandwich the anodes and resistive separators. The frame
 287 dimensions are 118 cm outer diameter, 112 cm inner diameter, with thickness 1.6 cm. The two rings,

288 and each amplification mesh and resistive spacer ring have 88 aligning drilled holes. A stack is formed
289 with one support frame on the bottom, followed by alternating the three amplification meshes with
290 the two resistive spacers and finished with the second support frame. Nylon bolts are passed through
291 the 88 drilled holes in the stack. Finally, on the side facing away from the camera readout, a hexagonal
292 aluminium stiffener is bolted to the framed assembly, attached to the nylon bolts at 16 of the 88 drilled
293 holes points.

294 The three anodes are constructed from steel meshes with 121 cm diameter. Anodes 1 and 2 are made
295 from 100 lpi meshes with a wire diameter of $27\ \mu\text{m}$. The optical transparency of the anode 1 and 2 mesh
296 is 89 %. The third anode is made from a 250 lpi mesh with $40\ \mu\text{m}$ diameter. We chose the meshes with
297 the smaller wire diameters for the two meshes closest to the field cage in order to achieve the highest
298 gas amplification in the first stages, and minimize the loss of light because of imaging the amplification
299 region through the cathode, anode 1 and anode 2 meshes. The meshes are epoxied to stainless steel
300 rings (outer diameter 118 cm, inner-diameter 112 cm, thickness 0.1 cm) after stretching the meshes as
301 described for the cathode. The procedure for stretching the anode meshes takes approximately a week
302 of successive stretching and relaxation of the mesh. Following this procedure, the average tension
303 force on the anode 1 and 2 meshes is $16.8\ \text{N cm}^{-1}$. The measured tension is uniform over the plane of
304 the anode mesh to better than 5 %. The average tension force on the anode 3 mesh is $38\ \text{N cm}^{-1}$. After
305 stretching, the meshes are epoxied to the stainless steel support ring in the same way as described for
306 the cathode [24]. The goal for the distance between the anode 1 and anode 2 (anode 2 and anode 3)
307 meshes is 0.5 mm (1 mm). A measurement of the capacitance of the amplification region is described
308 in Sec. 6.3.1. The capacitance measurement implies the distances achieved were approximately 1 mm
309 (2 mm) spacing. This is likely due to the epoxy and spacer thickness tolerances as well as flatness
310 variation.

311 Like the cathode, the amplification region assembly is supported on the three internal rails on the
312 pressure vessel using machined Delrin parts. These supports constrain the amplification region
313 distance to the closest field cage ring.

314 4.4. High-voltage distribution system

315 The anode meshes are provided with positive high voltage (HV) by either a CAEN NDT1470
316 or a CAEN N1470 multi-channel Power Supply (PS), which is controlled through a serial link over
317 USB. The cathode power supply is a Spellman SL 30 PS with a maximal output voltage of 30 kV. The
318 resulting limit on the electric field in the field cage is over $600\ \text{V cm}^{-1}$. The cathode PS voltage is
319 controlled by varying an analogue input from 0 to 10 V, which results in an output voltage from the PS
320 of 0 V up to its maximum voltage. This analogue signal is generated by the slow control system using
321 a LabJack U3-HV USB Data Acquisition (DAQ) device which is connected to the Spellman PS control
322 input.

323 The various meshes are connected to the power supplies through the following chain: Inside the
324 pressure vessel all meshes are connected to Kapton coated copper wires which in turn are connected
325 to the HV feed-throughs that pass through the pressure vessel wall. To provide extra insulation,
326 these wires have ceramic beads threaded along their entire length, and the resulting assembly is also
327 surrounded by a fibreglass sheath. In the case of the anodes the HV feed-throughs are rated to 10 kV;
328 in the case of the cathode the feed-through is rated to 20 kV. Outside the pressure vessel, each anode's
329 feed-through connects via coaxial cables to a custom 'bias box'. These bias boxes decouple the charge
330 signals from the constant current HV as shown in Fig. 6. Therefore each bias box connects to the
331 respective PS and each box has a signal output which is fed into the TPCs charge readout system.
332 Signals are routed from these signal outputs through a preamplifier, described in Sec. 4.5. The RC
333 constant of the R_{in} resistor and the respective mesh capacitance of $\sim 5\ \text{nF}$ as well as the RC constant of
334 the filter circuit limit the charge-up speed of the meshes and in turn help to quench discharges. The
335 output from these preamplifiers is fed into the detector's DAQ system which is described in Sec. 4.7.

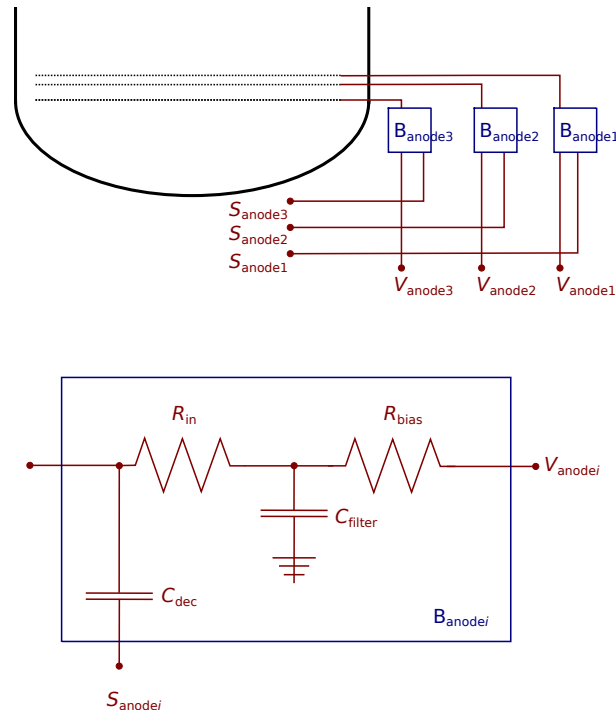


Figure 6. Schematic of the circuit to bring high voltage ($V_{\text{anode}i}$, $i \in 1, 2, 3$) to the anode meshes and to decouple the signal from the high voltage lines. The signals are decoupled in bias boxes via a 10 nF decoupling capacitor (C_{dec}) and are then fed to the signal line ($S_{\text{anode}i}$). These bias boxes $B_{\text{anode}i}$ feature also a protection and filtering circuit consisting of a bias resistor ($R_{\text{bias}} = 200 \text{ M}\Omega$), filter capacitor ($C_{\text{filter}} = 10 \text{ nF}$), and input resistor at the detector input ($R_{\text{in}} = 10 \text{ M}\Omega$).

336 The cathode feed-through is connected to a coaxial power supply cable using a custom Delrin
 337 assembly which separates the grounded outer conductor of the cable from the voltage carrying inner
 338 conductor. The grounds of the power supplies (both anode and cathode) are connected together in a
 339 grounding circuit which is coupled to the pressure vessel.

340 The voltages and currents supplied by each power supply channel are recorded by the detector's
 341 slow control system, for use in later analysis.

342 4.5. Charge signal measurement

343 The pre-amplifiers used for the detector's charge readout are charge-sensitive CREMAT CR-113
 344 (or CR-112) hosted in CR-150-R5 evaluation boards. The specified gains of the pre-amplifiers are
 345 1.3 mV pC^{-1} (or 13 mV pC^{-1} respectively). A measurement of the agreement of our preamplifiers with
 346 this value can be found in Sec. 6.3.1. The output signals from the preamplifiers are digitised by a CAEN
 347 N6730 8-channel digitizer, with 2 V dynamic range and 500 MHz sampling frequency.

348 4.6. Optical signal measurement

349 The optical readout system uses four FLI Proline PL09000 CCDs, each of which contains a
 350 front-illuminated Kodak KAF-09000 chip with 3056×3056 active pixels (9.3 Mp), and a pixel size
 351 of $12 \times 12 \mu\text{m}^2$. The chip has a quantum efficiency (QE) in the range of 50 – 70 % for photons with

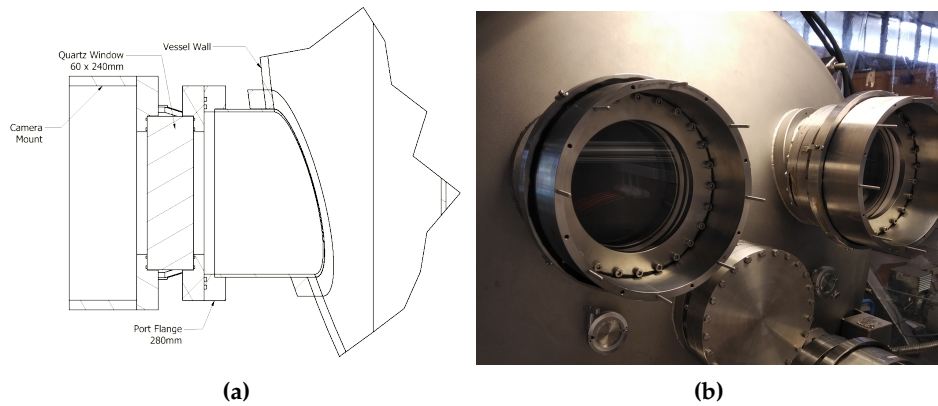


Figure 7. (a) Drawing of the optical flange with the camera mount. The thick quartz is necessary to ensure that the assembly can withstand the pressure difference between the vessel pressure and ambient pressure. (b) A photograph of the assembly with the camera removed.

352 a wavelength between 475 nm and 750 nm. In the wavelength range from 350 nm to 925 nm the QE
 353 is always larger than than 20%. These wavelength ranges cover the full VIS part of a spectrum
 354 and extend towards the NIR and UV, which makes the TPC sensitive in the regions of the spectrum
 355 discussed in Sec. 2.

356 Each camera's field of view is centred on a quadrant of the amplification plane. Each camera is
 357 coupled to a Nikon f/1.2 50 mm focal length lens with a 54.8° angle of view. The cameras are mounted
 358 to optical flanges as shown in Fig. 7. Quartz windows of 6 cm thickness are used to allow for the
 359 desired overpressure in the vessel. The transmission of the optical flanges is measured to be 97_{-4}^{+3} %
 360 for red light. The camera lenses have a transmission of 70 % (90 %) at 420 nm (750 nm) wavelengths,
 361 where the lens transmission includes all photons lost between the 7 elements of this compound lens.

362 Adding up the TPC drift distance, the non-active area between the cathode and the vessel door
 363 as well as the path through the camera assembly, the total object distance is approximately 102 cm
 364 which is larger than the minimum focal distance of our camera lenses. At this distance the system
 365 images a 71×71 cm field of view with a vixel size of $\sim 40 \mu\text{m}$, when no extra readout binning is
 366 applied. Considering the full optical path including quartz window and lens, we estimate a geometric
 367 acceptance of the optical system – the third term in brackets in Equation (1) – of approximately
 368 1.1×10^{-4} . Achieving a high enough gain in the amplification region to produce enough photons for
 369 signals to be detected above the noise, given this acceptance, is key.

370 To achieve optimal noise performance the CCDs are cooled to -25°C to -30°C . The cameras
 371 are equipped with an internal thermoelectric cooler which can cool the CCD to approximately 50°C
 372 below the ambient camera temperature. This is supplemented by a water cooling system attached to
 373 each camera to reduce its ambient temperature by 15°C . At -25°C operating temperature, the read
 374 noise per pixel is in the range of 9.6 to $11.3 e^-$, and the dark rate is $0.006 - 0.025 e^- / \text{pixel}/\text{s}$ (the range
 375 of variation is across the four cameras).

376 The CCDs digitize the number of electrons collected in each pixel in each exposure. For scale,
 377 the typical conversion gains of the cameras are $1.52 - 1.55 e^- / \text{ADU}$, where ADU is *analogue-to-digital*
 378 *units*. To mitigate the dominant effect of readout noise, pixels are grouped prior to digitization. This
 379 grouping reduces the noise per pixel in the group by approximately $1/\sqrt{N_{\text{pixels}}}$ given the relative
 380 scales of readout noise and dark current rate in a 1 s exposure. Typically we use 8×8 groupings
 381 ($N_{\text{pixels}} = 64$) as this gives an acceptable balance between readout noise and readout pixel size, with
 382 the effective vixel width (pixel width in the amplification plane) being approximately 2 mm.

383 4.7. *Slow control*

384 The slow control software sets and monitors the detector voltages, gas pressure and ambient
385 temperature. The software has a web based user interface, and uses java and C++ software to interface
386 with an SQL database. The database contains the values of the monitored variables as well as the
387 desired set points for these variables. The detector control code reads the set points from this database
388 and communicates with the high voltage power supplies to set the required voltage and read out the
389 measured voltage and current into the database. Control of the gas system is also achieved through
390 the same web interface, which is able to launch code communicating with the valve control hardware
391 to perform filling, venting and evacuation automatically.

392 4.8. *Data Acquisition*

393 The DAQ system triggers and acquires data from the charge and optical readout hardware.
394 DAQ commands are sent from the same web interface used for slow control to a DAQ PC which
395 communicates with the cameras and the CAEN N6730 digitiser used for the charge signals to initiate
396 each run. A run consists of a user-specified number of camera exposures (data frames), which are
397 acquired simultaneously from the four cameras as well as the charge waveforms digitized during the
398 exposure time. Additionally, at the start of the run a specified number of frames are acquired while
399 the camera shutters are closed. The use of these frames is to subtract off the baseline behaviour of
400 each pixel in the CCD chip when it is not exposed to light (Sec. 5.2). After these empty frames the data
401 frames are taken with the camera shutter open. The detector can run in two triggering modes. In the
402 first mode the data frames are taken immediately after each other, separated only by the CCD readout
403 time. In the second mode the data frames are taken based on an external trigger signal. During the
404 CCD exposure time the charge waveform digitiser (see Sec. 4.5) is triggered by signals larger or smaller
405 than a user-configurable threshold amount above the baseline on each channel, and then records
406 waveforms of typical duration 100 μ s around each trigger, including a configurable period of time
407 before the trigger event. The digitiser can also be triggered externally. In both triggering modes any
408 trigger causes all eight channels of the digitiser to be read out simultaneously. The DAQ system stores
409 the configuration of all of the parameters described in this subsection for each run.

410 5. **Optical Readout Analysis and Performance**

411 In this section we report on the results of data taking with ^{241}Am sources mounted in the pressure
412 vessel. The HPTPC was also tested using a beam at CERN, the analysis of which is ongoing and not
413 presented here. After explaining the CCD calibration (Sec. 5.1 and Sec. 5.2) we show a first scan of
414 various gas mixtures (Sec. 5.3) to establish the most promising mixture for a more comprehensive light
415 gain measurement. This in-depth measurement with a single mixture and its analysis is then shown in
416 Sec. 5.4.

417 Am-241 predominantly emits either a 5.486 MeV (84.8 %) or 5.443 MeV (13.1 %) alpha particle (α)
418 and different energy gamma-rays (γ), where the most probable ones have an energy of 59.54 keV or
419 26.34 keV [25]. Furthermore there is a substantial amount of x-ray radiation in the range from 10 keV
420 to \sim 20 keV. The α particles pass through a foil before they enter the gas volume, therefore their energy
421 is reduced by about 860 keV to \sim 4.56 MeV [26]. Such α particles are stopped inside the gas volume
422 and deposit their full remaining energy. The γ -rays have high enough energy to escape the active
423 TPC volume. According to a HEED [27] and GARFIELD++ [28] simulation which takes the HPTPC's
424 geometry into account only 1.2 % of all γ -rays interact in the counting gas. The lower energy x-rays
425 are more likely to interact; when integrating over all x-ray energies we find that 58 % are absorbed in
426 the active gas volume. Their overall contribution is still not large, since the ratio of the x-ray count
427 over γ -ray count is about 12 %. The emission distribution of the ^{241}Am in the forward hemisphere is
428 roughly isotropic for the different kinds of radiation. Furthermore there is a contribution from cosmic
429 rays.

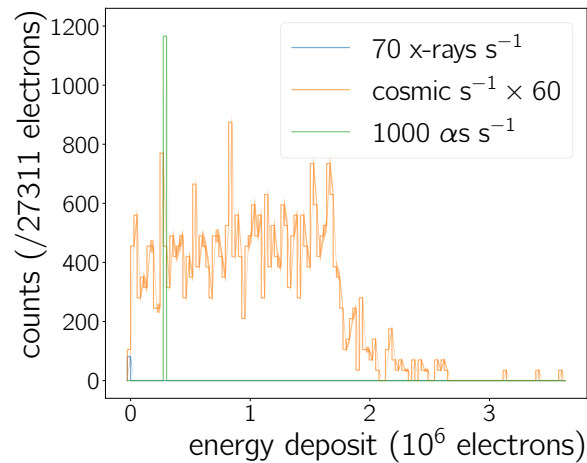


Figure 8. Simulated energy deposits of ^{241}Am decay radiation and cosmic muons inside a gas volume filled with Ar/CO_2 (90/10). Energy deposits are measured in the number of liberated electrons during the energy deposit. This is the result of a HEED [27] and GARFIELD++ [28] study taking into account the approximate layout of the HPTPC and the information in [25,26].

430 Figure 8 shows the result of a HEED and GARFIELD++ simulation of the expected energy deposits
 431 by these different sources of radiation, which does not take any trigger effects, electronic noise,
 432 gas gain or an amplifier response into account. For the simulation we assume a quadrant of the HPTPC's
 433 volume with a source location similar to the location in the experiment. The normalisation of the three
 434 different kinds of radiation in Fig. 8 is given by the result of the simulation: For 1000 Bq of ^{241}Am
 435 decays, all 1000 α particles interact in the active volume every second as do 70 x-rays and γ -rays. Note
 436 that the x-rays and γ -rays contribute only at the low energy end of the spectrum. The contribution
 437 from the cosmic rays per second is scaled up by a factor of 60 to make the shape of the cosmic ray
 438 spectrum better visible. The most distinct feature of the spectrum is the α -peak from the ^{241}Am
 439 at $\sim 175 \times 10^3$ electrons.^a For a gas pressure of 1 atm these ionisations are created along a 5 cm to 10 cm
 440 long trajectory, yielding a high ionisation density along the track. For larger pressures, the track length
 441 decreases and ionisation density increases. When amplified, this high ionisation density will result in
 442 many photons produced in a small area. An α particles' energy deposit in the detector is thus more
 443 easy to image with cameras than less ionising forms of radiation. Furthermore, a gain measurement is
 444 possible since the total energy deposited in the detector is known.

445 In the amplitude spectrum of the charge readout (*cf.* Sec. 6.3.2), we expect to see something qualitatively
 446 similar to the spectrum in Fig. 8. However, the simulation does not take into account the energy
 447 resolution of the amplification plane, hence the actual measured quantity – amplitudes or light
 448 intensity – will exhibit a spread larger than what is shown in the plot. Furthermore electronic noise is
 449 not included, which is a substantial contribution at threshold.

450 Two different configurations were used in our measurements: one using five ^{241}Am sources and one
 451 using a single ^{241}Am source. In the single source configuration the source is either visible in the overlap
 452 region of the top two cameras or the bottom two cameras. In the five source configuration the sources
 453 are arranged in a cross configuration and are distributed such that there are always two sources in
 454 the overlap region of two cameras and that the central source can be seen by all cameras. Occasional
 455 sparks can be used to map these positions in the recorded frames (Fig. 9a).

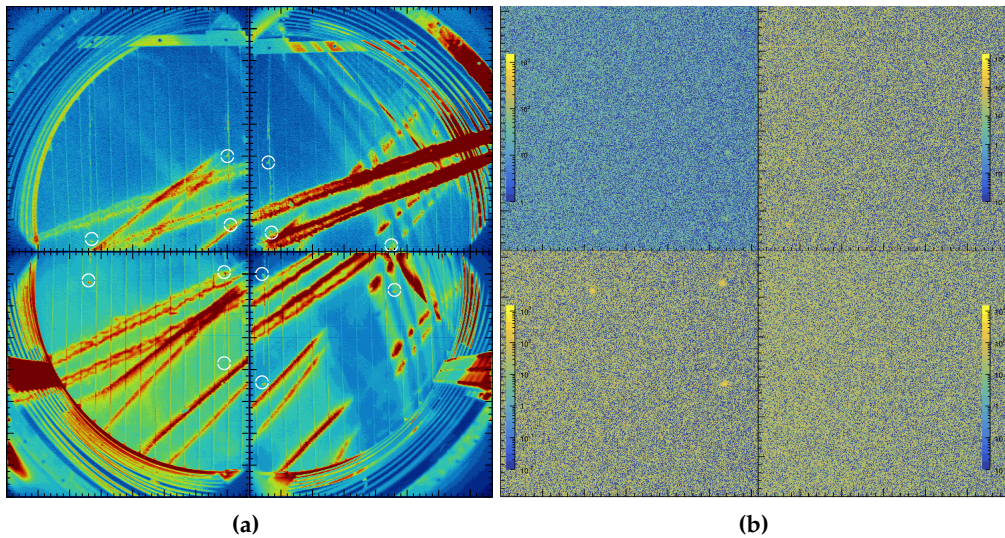


Figure 9. CCD images showing the readout plane of the HPTPC; the vertical (horizontal) image axis points along the y (x) direction. The colour encodes the light intensity in arbitrary units. (a) Simultaneously recorded frames during a spark event. The locations of the ^{241}Am sources (marked by circles) inside the TPC are visible during the spark event as well as the field cage rings and the anode support, cf. Fig. 5b. (b) Light yield from the calibration sources for 200 s exposure time in pure Argon at 3 bar absolute pressure. The intensity of the image in the top left frame differs from the other three frames, because the corresponding camera has a different conversion gain.

456 5.1. Spark Detection

457 A major source of noise comes from sparking in the chamber. These sparks mostly originated
 458 along the boltholes of the amplification region and from the cathode feedthrough. The frequency of
 459 these events increased with the anode and cathode voltages and ultimately limited the maximum
 460 voltages we were able to reach. Our gas mixture choices were thus driven by finding mixtures which
 461 allowed to operate the detector without many discharges at large enough voltages to see charge and
 462 light signals. The gas mixtures listed in Sec. 5.3 allowed us to operate the detector in a stable manner.
 463 Other gas mixtures as Ar/CF₄ were also tried out during the initial testing, but resulted in too many
 464 discharges to perform a light gain measurement and are hence not reported on.
 465 Sparks cause a large fraction of pixels in an image to become significantly brighter, an example is
 466 shown in Fig. 9a. The camera pixels measure charge in ADU. Images with sparking are rejected from
 467 the analysis as follows. First, events in which one of the CCD images has a pixel-value RMS above
 468 ~ 100 ADU to 300 ADU are rejected as sparks. Of the remaining images, those with events in which one
 469 or more of the CCD images have 100,000 pixels above 100 000 ADU are also removed from the analysis.
 470 The exact thresholds depend on the actual CCD camera and detector settings, e.g. the RMS thresholds
 471 vary from 133 ADU to 300 ADU between the four cameras. The exact values for each threshold have
 472 been identified by comparing the properties of spark images selected by eye to images without sparks.

473 5.2. CCD Camera Calibration

474 The CCD camera calibration removes variations in pixel gain, transient phenomena, and time
 475 dependent noise sources. The first step of the CCD calibration is the subtraction of *bias frames*, which
 476 deals with persistent features and noise sources, and accounts for variations in pixel gain. At the start

^a It turned out to be not feasible to simulate stopping of α particles in HEED. Therefore we ultimately simulated 11.8 MeV α particles, evaluated their most probable energy loss and scaled this energy loss to 4.56 MeV.

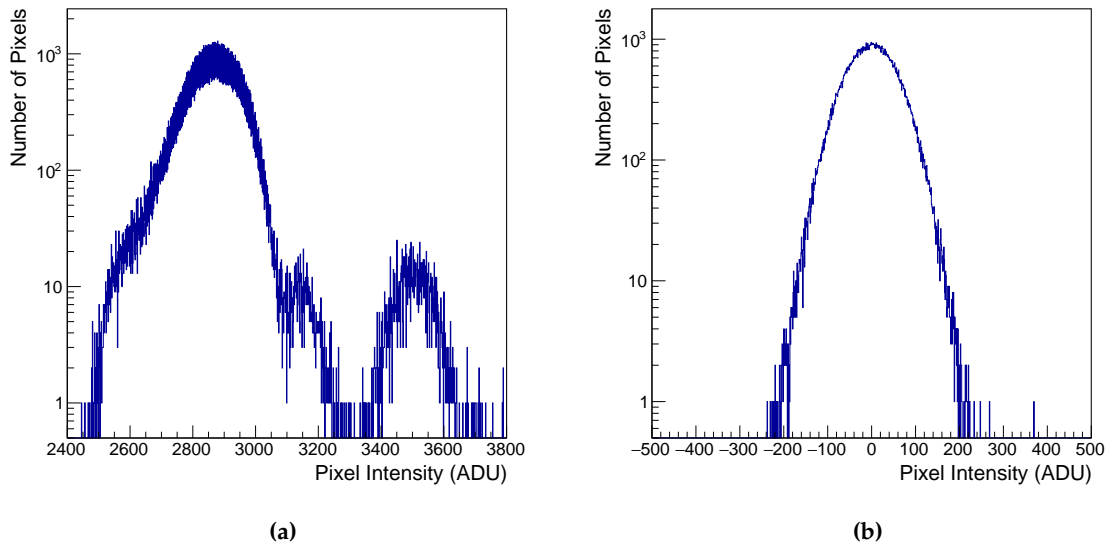


Figure 10. Analogue-to-Digital Unit (ADU) distribution of all pixels of an exposure frame before (a) and after (b) bias subtraction.

477 of each run we take 5–10 bias frames with the shutter closed. These are averaged and then subtracted
 478 from all *exposure frames* with shutter open in the same run, where a typical run consists of 20–100
 479 images (per camera) with an exposure time of 2 s per frame.

480 A source of transient noise is *hot pixels*, created *e.g.* by cosmic muons passing through the camera
 481 chip and saturating pixels. These hot pixels are usually confined to individual frames but can remain
 482 saturated over several exposure lengths. If they occur in the bias frames they must be corrected before
 483 the bias frame subtraction from the exposure frames. Each pixel value of each bias frame is compared
 484 to the values of the same pixel in the other bias frames, and if its ADU reading has changed by more
 485 than five standard deviations of its mean ADU value, the value of the pixel is set to that of the previous
 486 bias frame.

487 The next step of the CCD calibration is the temperature dependent image mean correction. The
 488 temperature of the CCDs is seen to increase with the number of events taken in a run. This results in a
 489 natural upwards drift in the pixels' intensities with time which contributes to the noise. This effect
 490 is corrected for by calculating each CCD frame's average pixel value and then subtracting that value
 491 from every pixel within that frame. This process is applied to every frame in all runs.

492 The impact of these calibration steps is to reduce the pixel intensity variance. The distribution of pixel
 493 values before and after bias subtraction is shown in Fig. 10.

494 5.2.1. Calibration without closed-shutter bias frames

495 The measurements in this paper are grouped into two data taking periods: One, where we explore
 496 different gas mixtures to find the most promising gas for an in depth measurement campaign (Sec. 5.3),
 497 and the second period where only the gas identified in the first period is studied (Sec. 5.4). During the
 498 beginning of the second period it was discovered that camera 2 (which was set up to take the light
 499 gain data) had a stuck open shutter. Due to time constraints we continued with data taking despite
 500 this and have adjusted our calibration accordingly as detailed in this section.

501 To address mechanical shutter failure, a procedure was developed to acquire bias frames for calibration
 502 with the shutter open. To avoid stray light from the sources or sparks, 1000 2 s shutter-open frames
 503 were acquired daily with the TPC voltages switched off. The anode meshes need to be slowly brought
 504 up to the desired voltages in order to reduce the probability of sparking and the subsequent need
 505 to reduce the voltages for some time. Reaching the target voltages in a gas mixture with low or no

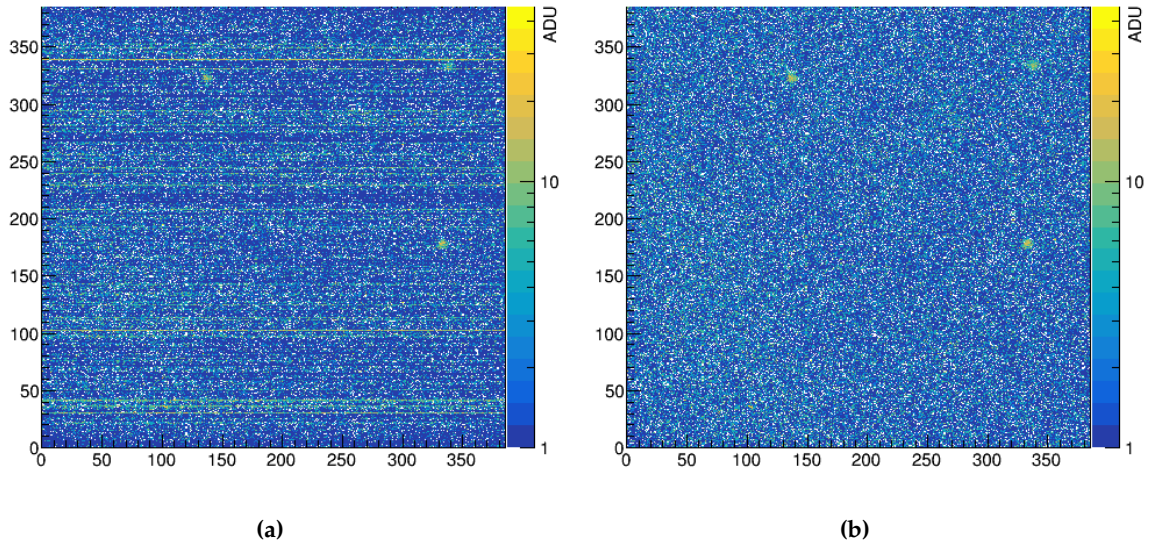


Figure 11. Example of the average of 100 bias subtracted events with event and bias frame taken days apart (a) before row correction (demonstrating row CCD artefacts) (b) after row correction (demonstration correction of row CCD artefacts). The colour in both plots encodes the ADU value at the position of a pixel, while the horizontal and vertical axis shows the y and x coordinate, respectively.

506 quencher content can thus take on the order of hours, when starting from zero. For this reason we
 507 decided to take these shutter-open bias frames not before every run. These frames are then used to
 508 produce a single, low noise *super bias* frame to be subtracted from each event taken that same day.

509 Super bias frame creation

510 The method used to create each super bias is to first remove any anomalous pixels by the method
 511 described in Sec. 5.2. Next, a 1D distribution for each pixel in the super bias is created and filled
 512 with the $N_{\text{bias}} = 1000$ ADU values measured by that pixel in all 1000 bias frames. The mean and
 513 standard deviation (σ_{pixel}) of that distribution is calculated and any ADU value above $3\sigma_{\text{pixel}}$ of the
 514 mean are removed. A Gaussian is fitted to the remaining 1D distribution of each pixel. The centre
 515 of the Gaussian gives the ADU value of that pixel in the super bias. As mentioned in Sec. 5.2, bias
 516 subtraction using a bias frame, taken close in time to the event frame can help to reduce temperature
 517 (and therefore time) dependent noise. Due to the significant time difference between bias and event
 518 frames additional corrections of temperature/time dependent effects need to be implemented before
 519 the super bias frame can be used as a bias frame for exposure frames.

520 Figure 11a shows an example of row pedestal artefacts. The scale of the effect has been artificially
 521 increased for demonstration purposes by using exposure and bias frames taken days apart. This effect
 522 occurs when the pedestal of each pixel within a row changes by some amount between taking the
 523 bias and exposure frame. These effects are not observed when the bias frames are recorded directly
 524 before the exposure frames as part of the same run, since the pedestal value shift occurs only between
 525 runs. In order to use the super bias frames we apply a row correction to every row in the super bias
 526 subtracted image. For this correction the average ADU value of a row is calculated whilst omitting
 527 any anomalous pixels or any pixels located within the region of interested for the analysis, *i.e.* the
 528 source locations. This average is then subtracted from each pixel in that row. Figure 11a shows the
 529 same image as Fig. 11b after row correction has been applied.

530 Applying row correction to a super bias subtracted image also corrects for any time dependent drift
 531 of pixel intensities (*e.g.* because of temperature). Figure 12 show an example of the pedestal drift in
 532 100 subsequent exposures (events) for 150 different runs before and after row correction. The bi-modal

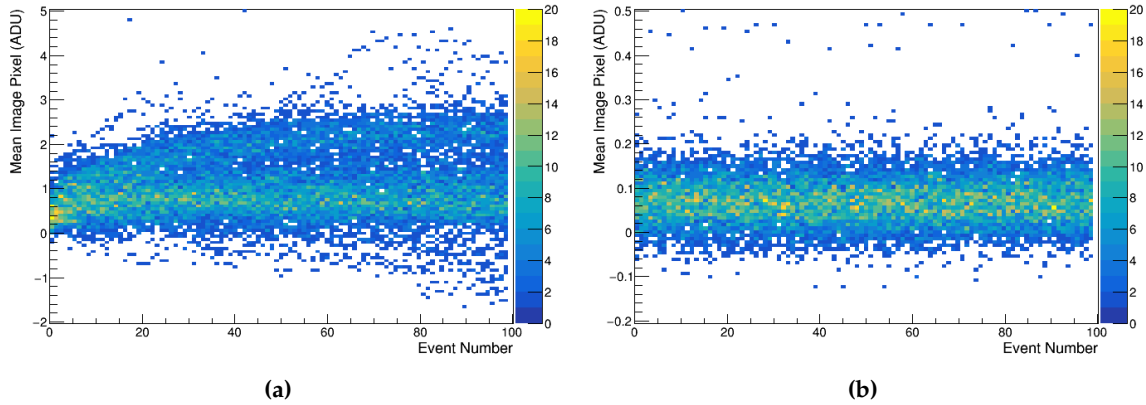


Figure 12. Mean ADU value of exposure frames versus event number for 150 runs (of 100 events, *i.e.* frames) taken over a number of days (a) before row correction (demonstrating pixel pedestal drift) (b) after row correction. The latter demonstrates the correction of the pedestal drift by the row correction procedure.

533 nature of Fig. 12a is likely due to temperature differences on different days. It should be noted that the
 534 row correction can fail for regions on the CCD where a differential pedestal drift is present. The lower
 535 left corner of the CCDs experiences such a non differential shift and care has been taken to ensure that
 536 the source positions do not overlap with affected rows.

537 Overall, super bias frame subtraction significantly reduces the pixel intensity variance in an event
 538 which is normally introduced by the classical bias frame subtraction, because the mean pixel value
 539 error in a super bias frame is reduced by $1/\sqrt{N_{\text{frames}}}$. When integrating a region of interest of 9×9
 540 pixels, *i.e.* $N_{\text{pixel}} = 81$, this 100% correlated uncertainty for a super bias frame constructed from 1000
 541 (bias) frames ($N_{\text{bias}} = 1000$) can be calculated using the following equation:

$$\sigma_{\text{bias}} = \sqrt{\frac{\sigma_{\text{pixel}}^2 \cdot N_{\text{pixel}}}{N_{\text{bias}}}} \quad (3)$$

542 For the standard deviation of a single pixel (σ_{pixel}) a typical value of 40 ADU can be used to estimate
 543 σ_{bias} . The resulting $\sigma_{\text{bias}} = 11.4$ ADU is significantly smaller as for *e.g.* the case where 5 bias frames are
 544 used.

545 5.3. Light Yields for Different Gas Mixes

546 An important question when operating gaseous detectors with optical readout is which gas
 547 mixtures will yield the most light from the interactions of interest. For this measurement light from a
 548 single ^{241}Am source in the overlap region of the top two cameras was used. Since the alpha particles
 549 from the decays travel only a few cm at the pressures considered (*cf.* the beginning of the section),
 550 a small region around the source location was considered for the light yield measurement. One of
 551 the cameras (top left, Fig. 9b) had a lower conversion gain than the other three so only the top right
 552 camera was used for this analysis. The trialed gas mixes were: pure argon (3 and 4 bar absolute),
 553 argon with carbon dioxide (4 bar absolute, Ar/CO₂ (99/1) and (99.25/0.75)), argon with nitrogen (3 bar
 554 absolute, Ar/N₂ (98/2)) and argon with nitrogen and carbon dioxide (4 bar absolute Ar/CO₂/N₂
 555 (98.75/0.75/0.50) and 4.9 bar absolute Ar/CO₂/N₂ (96/2/2)).

556 To determine the light gain the calibration procedures in Sec. 5.1 and Sec. 5.2 are applied to the
 557 relevant data runs. A 20×20 pixels ($\sim 3.8 \times 3.8 \text{ cm}^2$) region of interest around the source position is
 558 examined in the bias subtracted and calibrated exposure frames. All light recorded in the region of
 559 interest is integrated. The results of this study can be seen in Fig. 13. For each result presented in the

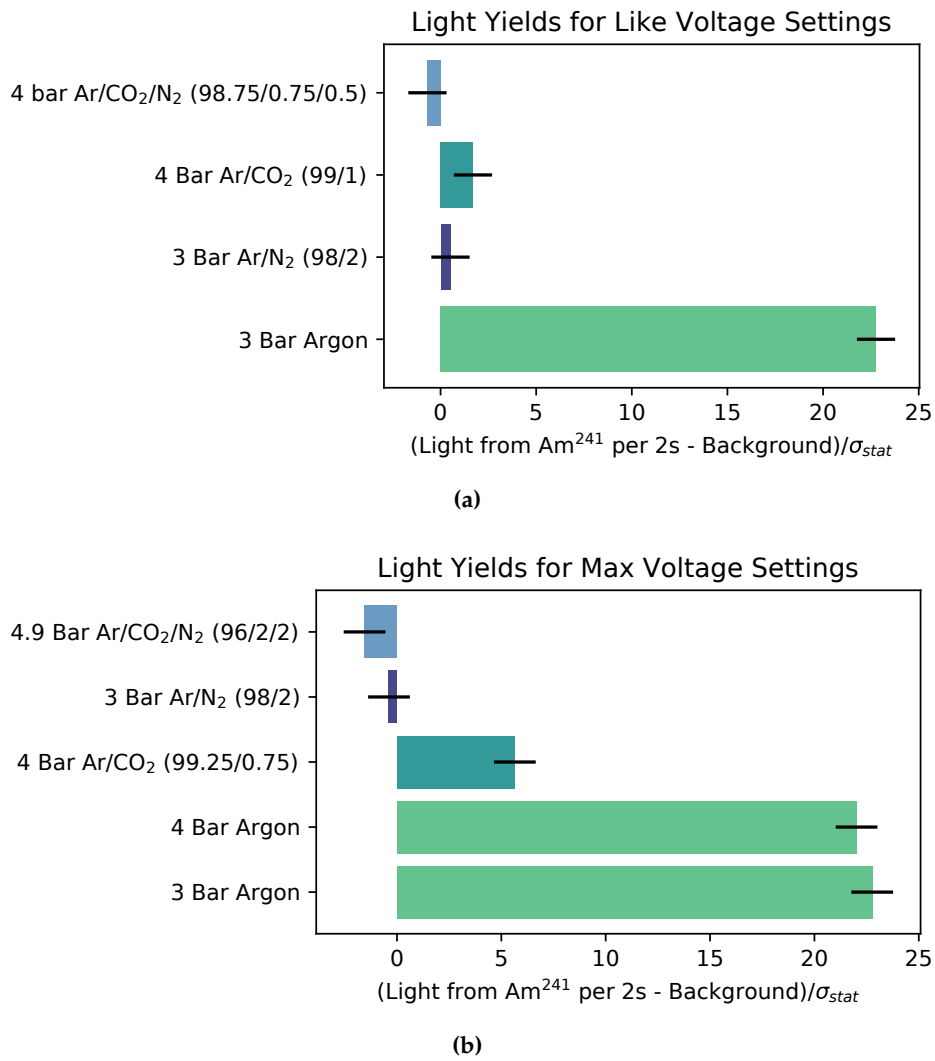


Figure 13. Light yield measured for an ^{241}Am source with different gas mixtures (a) at near constant anode and cathode voltages and (b) the maximal light yield achieved. The voltages used during these measurements are listed in Tab. 1.

(a)					
mixture or gas	P	V_{a1} [V]	V_{a2} [V]	V_{a3} [V]	V_c [V]
Ar/CO ₂ /N ₂ (98.75/0.75/0.5)	4 bar	1000	2000	4000	-7000
Ar/CO ₂ (99/1)	4 bar	1200	2400	4000	-7000
Ar/N ₂ (98/2)	3 bar	1200	2800	4000	-7000
Ar	3 bar	1500	2100	4500	-5250

(b)					
mixture or gas	P	V_{a1} [V]	V_{a2} [V]	V_{a3} [V]	V_c [V]
Ar/CO ₂ /N ₂ (96/2/2)	4.9 bar	3000	5900	7600	-8500
Ar/N ₂ (98/2)	3 bar	1550	3300	5000	-5000
Ar/CO ₂ (99.25/0.75)	4 bar	1200	2500	4800	-7000
Ar	4 bar	1000	1750	2800	-5700
Ar	3 bar	1500	2100	4500	-5250

Table 1. Voltage settings for the result plot shown in Fig. 13: (a) shows the voltages used for the settings shown in Fig. 13a, while (b) the settings used for the data in Fig. 13b. The absolute pressure is quoted.

560 two plots of Fig. 13 one data taking run has been used. All data is normalised to the same integrated
561 exposure time.

562 Two different comparisons were made, one at fixed anode voltages (Fig. 13a) and one at the maximum
563 anode voltages reached during stable operation (Fig. 13b). The voltage settings for both data sets are
564 shown in Tab. 1. In both cases the light yield from the ^{241}Am source was found to be highest in pure
565 argon. The pure argon results shows also that a high relative light gain can be achieved with lower
566 voltages as compared to the gas mixtures with a quencher. The high light gain of the 4 bar pure argon
567 measurement in Fig. 13b is surprising since intuitively a lower light gain than for the 3 bar gas mixture
568 would have been expected. Even more so as the voltages (normalised by pressure) applied during the
569 4 bar measurement are lower than in the 3 bar case. A saturation of the light gain at a given voltage
570 setting can explain such findings. Furthermore the fields during the 4 bar measurements could allow
571 for the incoming and amplified electrons to create more excitations and thus photons on the cost of
572 ionisations, as compared to the 3 bar case.

573 5.4. Light yield in argon at various voltage settings

574 Having identified pure argon as the brightest gas among the mixtures set out in Sec. 2, we now
575 examine how the optical gain in this gas is affected by the operational settings of our amplification
576 stage. Doing so we use pure argon at a pressure of 3 bar absolute, following the findings in the
577 previous section. Precisely how each of the multiple anodes contributes to the gain depends – among
578 other parameters as *e.g.* the voltage settings – on the anode’s relative alignment, which for meshes
579 is difficult to model analytically and numerically. The aim of the optical gain measurements in this
580 section is to understand how the light gain of the TPC is affected by **a)** the absolute voltage of the three
581 anode meshes V_{a1} , V_{a2} and V_{a3} when the potential difference between meshes is kept constant; **b)** the
582 potential difference between anode meshes 2 and 3 (ΔV_{a23}); and **c)** the potential difference between
583 anode meshes 2 and 1 (ΔV_{a12}). To do this we chose three voltage schemes which are as follows:

- 584 • Scheme A - Constant ΔV_{a12} and constant ΔV_{a23} ;
- 585 • Scheme B - Constant ΔV_{a12} and varied ΔV_{a23} ;
- 586 • Scheme C - Varied ΔV_{a12} and constant ΔV_{a23} .

587 To conduct a light measurement, a single ^{241}Am source is used, positioned so that it can be imaged by
588 camera 2, the bottom left camera. The source has an activity of 10 ± 1 kBq as has been determined by
589 an independent measurement, which was validated using ^{241}Am sources with known decay rates. An
590 exposure time of 2 seconds per frame was chosen to balance reduction of readout noise with reduction
591 in dead time due to lost frames from sparking.

592 5.4.1. Optical Gain Analysis

593 Schemes A, B and C (as described in the beginning of Sec. 5.4) consist respectively of 5, 11 and
594 9 integrated ADU measurements taken at different anode voltage configurations with step-sizes of
595 200 V or 400 V. Each voltage configuration has between 1000 and 1500 events with one frame per
596 camera each. Four sets of 1000 TPC-off shutter open bias frames were also taken to produce four
597 super bias frames. One taken before Scheme A and then one taken after each of the three schemes.
598 First the calibrations and checks detailed in Sec. 5.1 and Sec. 5.2.1 are applied. Doing so, all exposure
599 frames recorded within one voltage scheme are independently subtracted with the super bias frame
600 taken before and after the respective scheme. The more suitable super bias frame is selected for each
601 scheme based on the Gaussian nature of the pixels’ ADU distribution and on the flatness of the x and
602 y projections of the ADU distribution of frames within a scheme. Two super bias frames were selected
603 resulting in Schemes B and C sharing the same super bias frame.

604 Then a region of interest around the source is defined (referred to as *source box*). The source box’s size
605 is optimised to contain as few pixels as possible whilst not rejecting any signal. The analysis found
606 a nine by nine pixels ($16.56 \times 16.56 \text{ mm}^2$) source box to be optimal. After a loose pixel ADU cut, a

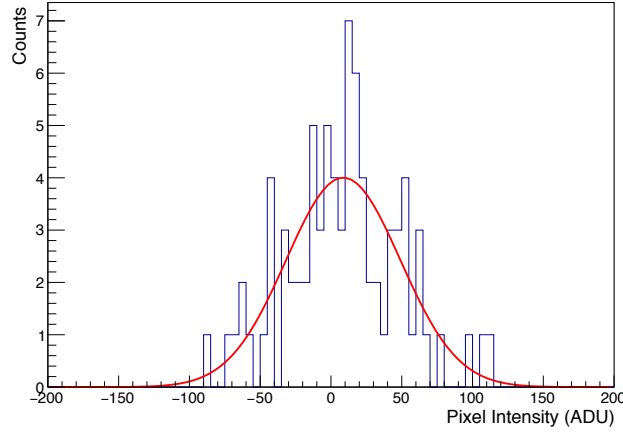


Figure 14. Intensity distribution of pixels within the source box for a single event.

607 Gaussian is fitted to the ADU values of the $N_{\text{pixel}} = 81$ pixels in the box for a given frame (as shown in
 608 Fig. 14). The integrated ADU per frame is then calculated by: $I_{\text{frame}} = \hat{\mu}_{\text{pixel}} \cdot N_{\text{pixel}}$, where $\hat{\mu}_{\text{pixel}}$ is the
 609 mean of the fitted Gaussian. The integrated ADU measurement for a run (I_{run}) is calculated by fitting
 610 a Gaussian to the distribution of I_{frame} values in that run. I_{run} is given by the mean of the fit and its
 611 uncertainty ($\sigma_{I_{\text{run}}}$) by the standard deviation on that mean. The final step takes the I_{run} values of the 10
 612 to 15 runs in each configuration and calculates their weighted mean (\bar{I}_w) and weighted standard error
 613 (σ_w). The mean and standard error for each voltage configuration are weighted by $w_i = 1/\sigma_i^2$ where σ_i
 614 is the standard deviation per run ($\sigma_{I_{\text{run}}}$) of the i^{th} run in the configuration. The weighted mean and
 615 weighted standard error are calculated as follows:

$$\bar{I}_w = \frac{\sum_{i=1}^{N_{\text{run}}} w_i I_i}{\sum_{i=1}^{N_{\text{run}}} w_i} \quad (4)$$

616

$$\sigma_w^m = \frac{\sigma_w}{\sqrt{N_{\text{run}}}} = \sqrt{\frac{\sum_{i=1}^{N_{\text{run}}} (I_i - \bar{I}_w)^2}{(N_{\text{run}} - 1) \sum_{i=1}^{N_{\text{run}}} w_i}} \quad (5)$$

617 where I_i is the integrated ADU value per run (I_{run}) of the i^{th} run in the configuration, N_{run} is the total
 618 number of runs in the configuration and σ_w is the weighted standard deviation. \bar{I}_w and σ_w^m give the
 619 final integrated ADU value of the voltage configuration (I_{config}) and its uncertainty ($\sigma_{I_{\text{config}}}$). In theory
 620 one could calculate $\sigma_{I_{\text{config}}}$ without the intermediate step of calculating I_{run} . However, examining I_{run}
 621 ensures that run to run instabilities are accounted for in the the uncertainty of the final measurement.
 622

623 5.4.2. Light gain as function of voltage

624 The final results of the light gain measurements can be seen in Fig. 15. In Scheme A, shown in
 625 Fig. 15a, the potential differences between the three anode meshes are held constant at 1200 V while
 626 the voltages of all three are varied in 200 V steps. Scheme A is consistent with the light gain having
 627 no dependence on the absolute voltage of the three anodes while ΔV_{a12} and ΔV_{a23} are fixed at 1200 V,
 628 suggesting the amplification is driven by the voltage differences between the anode meshes. Across all
 629 Scheme B voltage configurations, shown in Fig. 15b, $V_{a1} = 1200$ V and $V_{a2} = 2400$ V respectively, while
 630 V_{a3} and thus ΔV_{a23} , is varied. Scheme B shows a clear linear dependence of light gain on ΔV_{a23} over
 631 the range 0 V to 2500 V with a gradient of 0.074 ± 0.005 ADU/V ($1.50 \pm 0.01 \times 10^{-4}$ ADU/(V/m)).
 632 Across all Scheme C (Fig. 15c) voltage configurations V_{a1} and ΔV_{a23} are equal to 1200 V, whilst ΔV_{a12}
 633 and thus V_{a2} and V_{a3} are varied. The results of Scheme C suggest the light gain has a positive linear

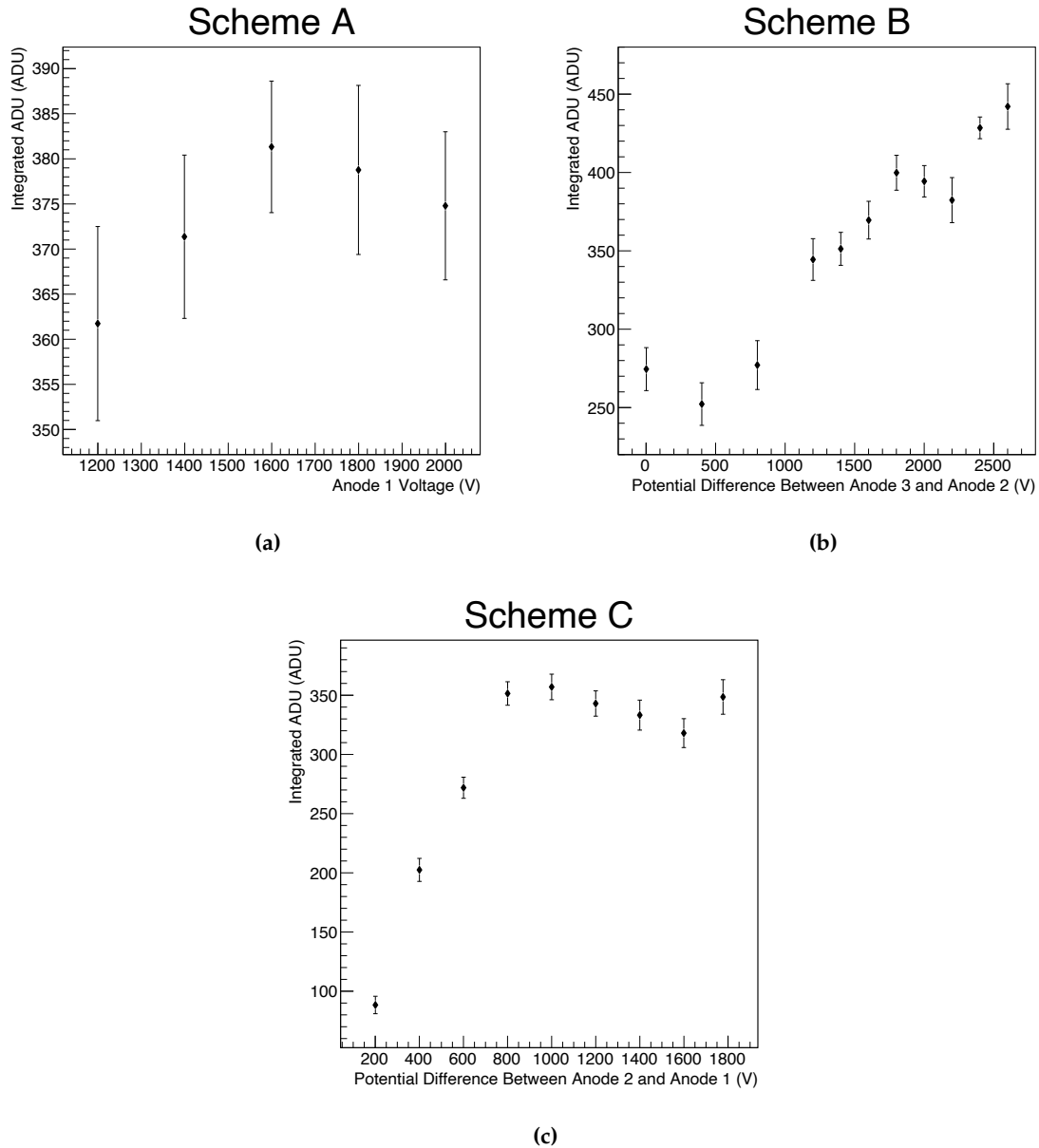


Figure 15. Light gain measurements of integrated ADU from ^{241}Am source (a) vs anode 1 voltage where the voltage difference between anode 1 and 2 (anode 2 and 3) is kept constant at $\Delta V_{a12} = \Delta V_{a23} = 1200\text{ V}$, (b) vs voltage potential difference between anode 2 and anode 3 whilst the voltage difference between anodes 1 and 2 is maintained at 1200 V , and (c) vs potential difference between anodes 1 and 2 whilst the potential difference between anode 2 and 3 is maintained at 1200 V . The figure is shown with a logistic function fit which is chosen on an empirical basis. All measurements have been performed in the same fill of pure argon at 3 bar absolute pressure.

634 dependence on ΔV_{a12} up to ~ 800 V where the light gain plateaus to a value of 343.0 ± 4.7 ADU. The
 635 gradient of this linear region is 0.45 ± 0.04 ADU/V ($3.75 \pm 0.04 \times 10^{-4}$ ADU/(V/m)) when fitting a
 636 first order polynomial to the first four points of the scheme.

637 We speculate on the origin of the plateau after ~ 700 V observed in Scheme C. One hypothesis is that
 638 the plateau occurs when the electric field between anodes 1 and 2 (E_{a12}) equals that between anodes
 639 2 and 3 (E_{a23}). When $E_{a12} > E_{a23}$ fewer electrons will be able to move from the gap between anode
 640 1 and anode 2 into the gap between anode 2 and 3 and thus there are fewer electrons available for
 641 amplification and/or excitation. The analysis of the circuit response and the inferred capacitances
 642 (Sec. 6.3.1) suggest that the distance between anode 1 and 2 is 1.20 ± 0.05 mm and the distance between
 643 anode 2 and anode 3 is 2.0 ± 0.2 mm. Using these distances we obtain $E_{a12} = 5.83 \pm 0.87$ kV cm $^{-1}$ and
 644 $E_{a23} = 6.0 \pm 0.6$ kV cm $^{-1}$. As both value agree with each other, we find $E_{a12} = E_{a23}$ where the plateau
 645 occurs. The fact that the rise in light gain stops when $E_{a12} = E_{a23}$, could thus be related to a change in
 646 electron transparency of anode 2. Observing a plateau and not a simple drop in the light gain's gradient
 647 with increasing voltage is however surprising, because for a plateau to arise the hypothesised electron
 648 loss needs to be exactly compensated by an increased light yield from the electrons in the anode 1 and
 649 2 gap. During the Scheme B measurements E_{a12} was held at a value of 10.00 ± 4.16 kV cm $^{-1}$, using
 650 the distances discussed before. E_{a23} was scanned from 0 to 13.0 ± 1.3 kV cm $^{-1}$. $E_{a23} > E_{a12}$ is fulfilled
 651 from a ΔV_{a23} of 2000 ± 200 V onwards and a plateau should be visible as in the case of Scheme C. The
 652 data in Fig. 15b is not sufficient to conclude that the trend reaches a plateau at said value nor the
 653 opposite as the plateau's expected position is too close to the end of the ΔV_{a23} voltage scan. With the
 654 maximal E_{a12} in its error-bars, a ΔV_{a23} of 2800 V would be required to reach the cross over between the
 655 rising and the plateau region.

656 The conclusion drawn from this study is that the light gain in the amplification region depends most
 657 strongly on the potential differences between the meshes, rather than the absolute voltage on the mesh
 658 wires.

659 5.4.3. Number of Photons in Amplification Region Per Primary Electron

660 In order to calculate how many photons are produced in the amplification region per primary
 661 electron in the drift volume it is necessary to make use of additional measurements and some
 662 assumptions. In this work we do not attempt to calculate the relationship between primary electrons
 663 in the drift volume and the number of electrons in the amplification region directly (by considering
 664 diffusion, mesh transit and charge gain) as we cannot externally constrain all the variables. Instead we
 665 calculate the number of photons per second in the amplification region (N_γ) from the ^{241}Am source
 666 using the observed ADU in the CCD as follows:

$$N_\gamma = \frac{\text{ADU}_{\text{obs}}}{(\text{Conversion Gain}) \times QE^*(\varepsilon) \times \Omega \times [T_{\text{window}} \times T_{\text{lens}} \times T_{\text{cathode}} \times T_{\text{anode}}^2]}$$

667 where ADU_{obs} is the observed ADU from the CCD per second in the region around the source. In
 668 our measurements the maximum value reached was 225 ± 10 ADU/s, cf. Fig. 15b divided by the
 669 exposure time of 2 s. The conversion gain provided by the manufacturer is 1.5 ADU per electron.
 670 The quantum efficiency QE^* is a function of the incident photon energy, for light in the near infrared
 671 the manufacturer specifies $60 \pm 10\%$ of photons converted into electrons. In principle we could be
 672 seeing light in the visible, infrared and ultraviolet from the argon scintillation. However, since both
 673 the quantum efficiency of the CCD and the transmission probability through the quartz windows has
 674 a rapid drop off below 350 nm we assume in this calculation that we are not sensitive to the UV light.
 675 Some photons will not make it from the amplification region to the CCD. The geometric acceptance of
 676 the system, Ω was calculated to be $(1.1 \pm 0.11) \times 10^{-4}$. $T_{\text{lens}} = 80 \pm 10\%$ and $T_{\text{window}} = 97_{-4}^{+3}\%$ are
 677 the transmission probabilities through the lens and quartz window respectively. In addition, all of
 678 the photons imaged from the amplification must pass through at least one cathode and one anode
 679 mesh, with the majority of them passing through two anode meshes. The transmission probabilities

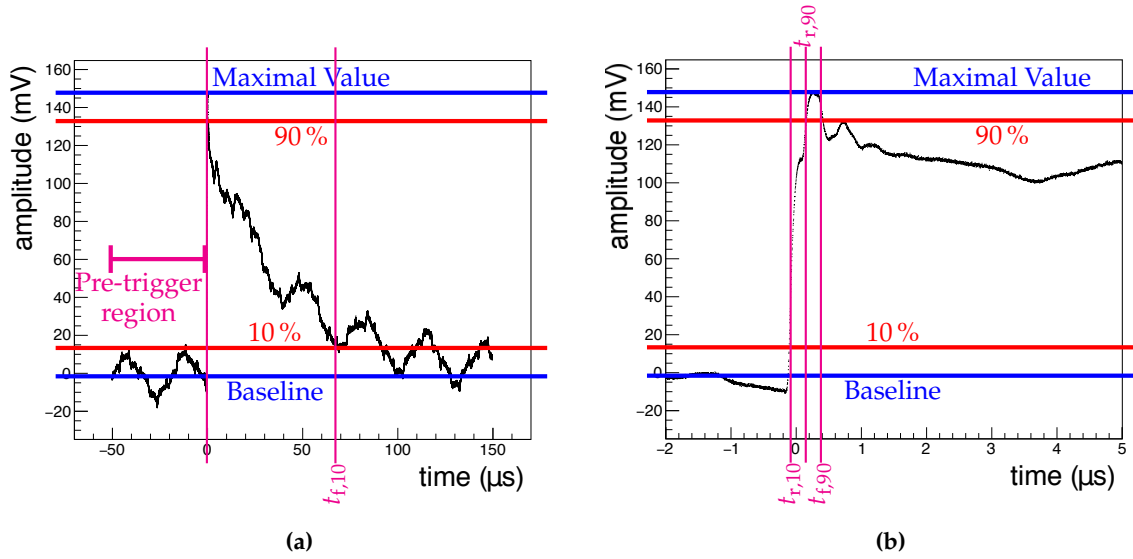


Figure 16. Example for a charge signal, a waveform – (a) and (b) zoom – with some of its defining features indicated. See the text for more explanations. The first vertical line in Figure (a) shows the approximate position of all the vertical lines in the zoomed plot in (b).

680 through the cathode and anode meshes are $T_{\text{cathode}} = 0.97$ and $T_{\text{anode}} = 0.89$ respectively. This results
 681 in $N_{\gamma} = (3.8 \pm 0.7) \times 10^6$ photons per second in the amplification region.

682 We then make a calculation of the expected primary electrons in the drift volume per second, N_e , based
 683 on the measured activity of our ^{241}Am source as follows:

$$N_e = N_{\alpha} \times \frac{\langle \varepsilon_{\alpha} \rangle}{W}$$

684 where $N_{\alpha} = 10 \pm 1\text{ kBq}$ is the activity of our alpha source and $\langle \varepsilon_{\alpha} \rangle = 4.56\text{ MeV}$ is the expected energy
 685 deposited by the alpha particles after exiting the source and the energy required for ionisation in argon
 686 is $W = 26.4 \pm 0.3\text{ eV/electron}$. This results is $N_e = (1.7 \pm 0.2) \times 10^9$ electrons per second in the imaged
 687 part of the drift volume. Combining these two results we expect there to be a total of $(2.2 \pm 0.5) \times 10^{-3}$
 688 photons in the NIR in the amplification region per primary electron in the drift volume.

689 6. Charge readout analysis and performance

690 In this section, we discuss the raw data obtained from the charge readout and the analysis which
 691 turns this raw data into physical quantities. We explain the calibration of the TPC charge readout
 692 with radioactive sources and cosmic radiation, and report the charge gain obtained with different high
 693 voltage settings.

694 6.1. Anatomy of a waveform

695 Signals from the three anode meshes are decoupled from their respective HV line as described in
 696 Sec. 4.5, fed into a pre-amplifier, and digitised. Figure 16 shows an example of a digitised waveform,
 697 as a trace of voltage versus time. We define the quantities V_i and t_i to be the digitised voltage and time,
 698 respectively, at the i^{th} time sample.

699 A waveform is comprised of three characteristic regions in time, shown on the sample waveform: the
 700 period before the digitiser has triggered (*pre-trigger*), the time at which the digitiser triggered and the
 701 period after (*post-trigger*). The pre-trigger region – that is, sample 1 to sample $N_{\text{pre-trig}}$ corresponding
 702 to $t = 0$ – is used to calculate a mean baseline (*Baseline* in Fig. 16) and baseline RMS for a waveform.

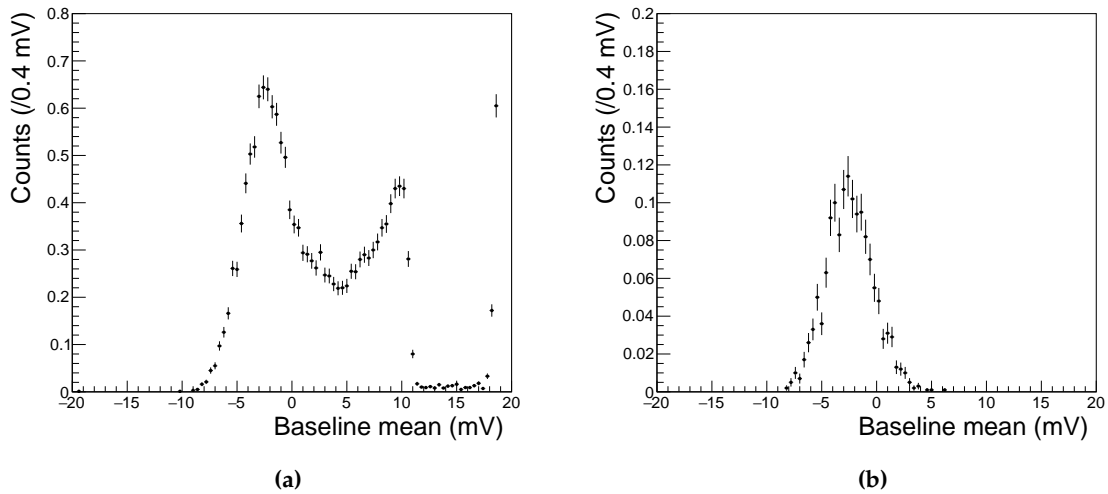


Figure 17. Anode 1 *Baseline* spectrum (a) before cleaning, and (b) after cleaning. Waveforms with large *Baseline* values are cut, which removes spark events.

703 The pre-amplifiers are charge-integrating; thus the maximum voltage of the charge waveform
 704 is proportional to the total charge collected on an anode. The amplitude (negative amplitude) of a
 705 waveform is taken to be the largest (smallest) V_i value of the waveform, $\max(V_{i=0\dots N})$ ($\min(V_{i=0\dots N})$),
 706 subtracted by the mean baseline. We distinguish properties of negative polarity pulses from positive
 707 ones by adding a *negative* where appropriate to the respective property's name.
 708 The start-time ($t_{r,10}$ in Fig. 16b) of a pulse is found by looking backwards in time (examining samples
 709 with decreasing sample number i) from the sample with the maximum (minimum) V_i value to the point
 710 in time where the waveform reaches 10% of its amplitude value. The point at which the waveform
 711 reaches 90% ($t_{r,90}$ in Fig. 16b) of its amplitude is identified in the same manner. From the maximum
 712 voltage, the waveform decays exponentially with a time-constant depending on the pre-amplifier chip
 713 used. Likewise, the $t_{f,10}$ and $t_{f,90}$ points on the tail of the waveform are found by finding the point
 714 after the maximum (minimum) where the amplitude first falls below 90% and 10% of the peak value.
 715 A pulse's rise time (fall-time) is calculated as the difference between $t_{r,10}$ and $t_{r,90}$ ($t_{f,90}$ and $t_{f,10}$).
 716 In addition to the above the RMS of a charge waveform is calculated as:

$$\text{WaveformRMS} = \sqrt{\frac{1}{N} \sum_{i=1}^j V_i^2} \quad (6)$$

717 where j is the number of the last sample. The *BaselineRMS* is calculated in a similar manner, but only
 718 taking V_i in the pre-trigger region into account.

719 6.2. Waveform cleaning

720 In order to get the most accurate values of the parameters described above, we apply a series of
 721 cleaning steps to the waveforms before calculating the parameters. Cuts are made to select waveforms
 722 based on their *Baseline* and *BaselineRMS*. The mean of the *Baseline* values of all waveforms in a run
 723 is calculated. If the baseline mean of a waveform is not within a 5 RMS interval of the mean of all
 724 *Baseline* values, the waveform is rejected. Similarly, if the *BaselineRMS* of waveform is not within a
 725 5 RMS interval of the mean of all *BaselineRMS* values, the waveform is cut. This cut allows to remove
 726 all waveforms with anomalous fluctuations of the baseline, as occur *e.g.* during sparks. Figure 17
 727 shows a spectrum of the anode 1 *Baseline* values before and after applying these cuts.

728 Waveforms with a *Baseline* above the trigger threshold are cut. Furthermore, a set of simultaneously
 729 recorded waveforms is rejected when the maximum V_i value of the anode 3 waveform is below the

Cut	surviving signals	
	single cut	cuts applied subsequently
No Cuts	100 %	100 %
$Baseline < \text{Trigger-threshold}$	99.97 %	99.97 %
$Baseline$ within mean interval	99.97 %	99.97 %
$BaselineRMS$ within interval	99.99 %	99.97 %
$\max(V_i) > \text{Trigger threshold}$	11.25 %	11.23 %
rise time $< 5 \mu\text{s}$	61.23 %	9.59 %
$Peak Time < 5 \mu\text{s}$	20.56 %	9.59 %

Table 2. Fraction of analysed waveforms rejected for each data cleaning cut for a run where no sparking was observed.

Cut	surviving signals	
	single cut	cuts applied subsequently
No Cuts	100 %	100 %
$Baseline < \text{Trigger-threshold}$	53.26 %	53.26 %
$Baseline$ within mean interval	26.85 %	26.85 %
$BaselineRMS$ within interval	68.29 %	26.85 %
$\max(V_i) > \text{Trigger threshold}$	5.64 %	5.22 %
rise time $< 5 \mu\text{s}$	51.53 %	4.35 %
$Peak Time < 5 \mu\text{s}$	14.92 %	4.25 %

Table 3. Fraction of analysed waveforms rejected for each data cleaning cut for a run containing spark events.

730 trigger threshold. This is because we trigger the simultaneous readout of all three anodes with the
731 anode 3 signal. In cases where only the anode 3 waveform's maximal V_i is above its trigger threshold,
732 the corresponding anode 1 and 2 waveforms can still be used in an amplitude measurement.
733 Checks are made to identify events containing sparks and such events with a damaged pre-amplifier.
734 An "event" contains all waveforms recorded during the exposure time of the simultaneously taken
735 CCD frames. In case of sparks the pre-amplifiers' baselines moves substantially and it takes time for
736 the pre-amplifier to return to the pre-spark status. Thus an event is flagged as spark event when it
737 contains more than 5 waveforms with a $Baseline$ above the trigger threshold. When a pre-amplifier gets
738 damaged the result is flat waveform. So we flag events where the maximum value is very close to the
739 baseline ($\max(V_i) < Baseline \times 1.02$) and ($\max(V_i) > Baseline \times 0.98$) as having been taken with a
740 damaged preamp.
741 Finally, waveforms are accepted or rejected based on their rise time and $Peak Time$. The $Peak Time$ is
742 the time value t_j in a waveform for which $V_j = \max(V_i), i \in 0 \dots N$. We calculate the rise time as the
743 time difference between: $t_{r,90}$ and $t_{r,10}$. For anodes 2 and 3, waveforms with a rise time above $5 \mu\text{s}$ or
744 a $Peak Time$ which is not within a $5 \mu\text{s}$ interval around $t = 0$ are cut. For anode 1, the peaks are not
745 always visible above the noise. Waveforms with a long rise time or a $Peak Time$ outside of $t < \pm 5 \mu\text{s}$
746 are rejected for the anode 1 amplitude measurement, but the corresponding waveforms in anode 2 and
747 3 are not cut. These time values are conservative cuts, chosen far above the pre-amplifiers specified
748 rise time of 3 ns, which help to remove waveforms which have been triggered by noise. Table 2 and
749 Tab. 3 show the fraction of analysed waveforms rejected by each data cleaning cut.

750 6.3. Gas gain measurement

751 In this section the charge gain of the three anode amplification stage is calculated from the
752 amplitude spectra discussed above. Features in the spectra have to be related to a known energy
753 deposition inside the HPTPC. A known energy deposit can be realised using a radioactive source
754 e.g. ^{241}Am (cf. Sec. 5). Primary ionisation electrons (Q_e) from converted γ -rays or α particles drift
755 towards the anode meshes and are amplified there. The amplification factor, the charge gain of the
756 amplification region G_{amp} , depends on the meshes' configuration such as inter mesh distance and HV

Measurement taken	Capacitance's between Anode 1/2 [nF]	χ^2/N_{dof} of Anode 1/2	Capacitances between Anode 2/3 [nF]	χ^2/N_{dof} of Anode 2/3	Capacitances between Anode 1/3 [nF]
fit	7.3 ± 0.3	0.76	4.4 ± 0.4	0.35	-
Multimeter reading	6.06 ± 0.05	-	3.72 ± 0.05	-	2.16 ± 0.05

Table 4. Mesh capacitances determined by a fit [29] and by a direct measurement with a multimeter.

757 settings. After charge signals are decoupled from the HV line, they are amplified by the pre-amplifiers
758 (G_{preamp}). The amplitude A of a waveform thus relates to Q_e as

$$A [\text{mV}] = f \cdot G_{\text{preamp}} [\text{mV pC}^{-1}] \cdot G_{\text{amp}} \cdot Q_e [\text{pC}] \quad . \quad (7)$$

759 The factor f is another dimensionless factor which we introduce in order to describe (attenuating)
760 effects of the readout circuit on the signal height. G_{preamp} and f are determined with dedicated
761 measurements to calibrate the readout circuit.

762 6.3.1. Pre-amplifier and circuit calibration

763 The pre-amplifier chips employed are Cremat CR-112 and CR-113 charge sensitive pre-amplifiers,
764 hosted on a CR-150-R5 evaluation board. The gain of the pre-amplifier chips is calibrated by injecting
765 pulses into the evaluation board test input (1 pF input capacitance). We chose rectangular pulses
766 with a pulse height V_{input} , and a low frequency and long width as compared to the pre-amplifiers
767 decay time of a few 100 μs . These pulses are recorded with the HPTPC's data acquisition system
768 and analysed with the analysis chain described above, but without applying cleaning since no noise
769 signals are present when not applying HV to the detector. For a given test pulse height, the resulting
770 amplitude spectrum features one peak. The ratio of the peak's mean amplitude to the input pulse
771 height gives G_{preamp} when taking the pre-amplifiers input capacitance into account. Testing several
772 chips, the average gain of the CR-112 chips is measured to be $G_{\text{preamp}}^{\text{CR-112}} = 11.7 \pm 0.6 \text{ mV pC}^{-1}$, and the
773 average gain of the CR-113 chips was measured to be $G_{\text{preamp}}^{\text{CR-113}} = 1.24 \pm 0.06 \text{ mV pC}^{-1}$. These values
774 are consistent with the values provided by the supplier of 13 mV pC^{-1} and 1.3 mV pC^{-1} , respectively.

775 A detailed description of the HPTPC's circuit response to test pulses can be found in [29]. To perform
776 these tests one of the three pre-amplifiers is disconnected from its bias box ($S_{\text{anode}i}$ in Fig. 6) and
777 test pulses are injected where it is usually connected. Doing so induces signals on the other two
778 anode meshes, which are read out. Table 4 shows the inter-mesh capacitances measured with a digital
779 multimeter as well as the results from a fit to the data obtained during the test-pulse campaign. The
780 capacitance determined by measuring pulse amplitudes and by multimeter measurement differ by
781 17%. This difference is likely due to the fact that the multimeter measurement is performed close to
782 the detector, *i.e.* no long cables and other parasitic capacitances are present. The distance between the
783 mesh planes can be determined knowing the capacitances:

$$C = \epsilon_0 \frac{A}{d}, \quad (8)$$

784 where C is the capacitance, ϵ_0 the vacuum permittivity, A the area of the mesh planes and d the distance
785 between two mesh planes. This assumes that the meshes can be approximated as a parallel plate
786 capacitor. Inserting our mesh geometry into the calculations in [30] shows that such an approximation
787 overestimates (underestimates) the actual capacitance (mesh distance) by less than 10%. Furthermore
788 we use $\epsilon_{\text{Ar}} = 1$ which is accurate to a level better than 1% [31], hence $\epsilon_{\text{Ar}}\epsilon_0 = \epsilon_0$. We can calculate
789 that anode 1 and 2 are $1.20 \pm 0.05 \text{ mm}$ apart and the distance between anode 2 and anode 3 is 2.0 ± 0.2
790 mm. These values are likely too small, since the used approximation underestimates the distance as
791 mentioned before. During construction we aimed for a spacing of 0.5 mm (1 mm) between anode 1
792 and 2 (anode 2 and 3) (*cf.* Sec. 4.3). The values determined here have the right order of magnitude and

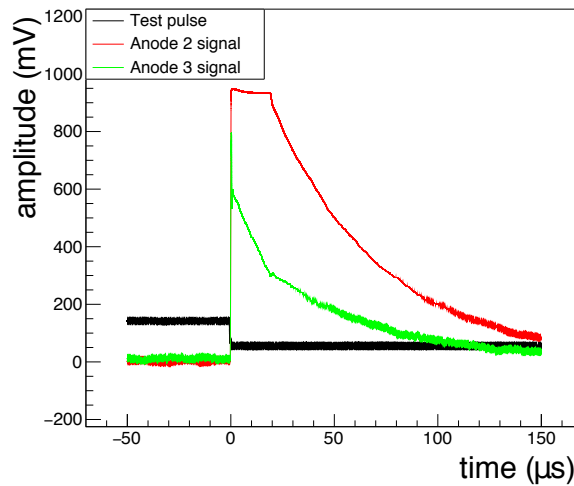
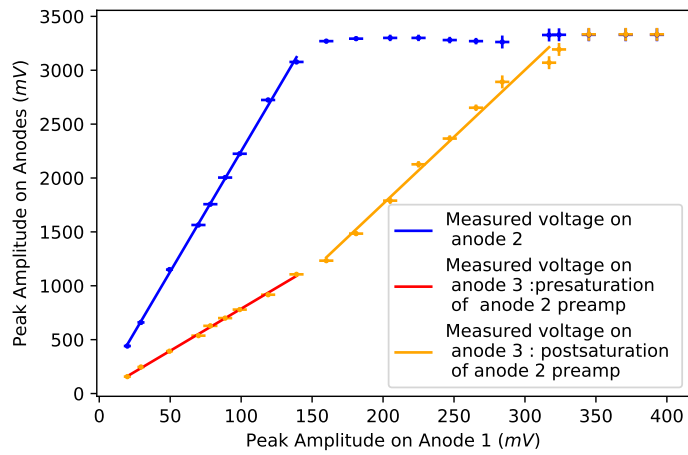


Figure 18. Waveform of a test pulse, coupled into the anode 1 mesh and the resulting amplified pulses (CR-112) as digitised by the HPTPC’s data acquisition system.

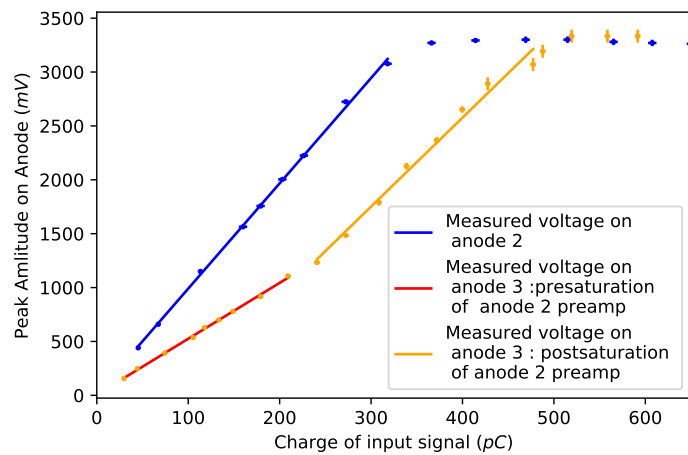
793 are close to the design values. The difference can be due to the fact that the exact thickness of the glue
 794 layers in the amplification region is not known, therefore the design values are most likely a lower
 795 limit.

796 Figure 18 shows an example where a test pulse is coupled into S_{anode1} at the anode 1 bias box while the
 797 anode 2 and anode 3 signals are amplified and digitised. In the figure the anode 2 signal is saturated,
 798 whilst the decay of the anode 3 signal shows a change of decay constant around $\sim 20 \mu\text{s}$. A systematic
 799 study of the amplified signals’ peak height ($V_{\text{output}}^{\text{amp}}$) revealed that as soon as one pre-amplifier is
 800 saturated, the signal on the other pre-amplifier shows a modified decay similar to what is visible
 801 in Fig. 18 [29]. This behaviour affects the measured amplitude as shown in Fig. 19: The points for
 802 anode 2 feature two distinct regions: An initial region of linear increase up until an output voltage of
 803 $3330 \pm 20 \text{ mV}$ where the pre-amplifier saturates and the region after that. The saturation value is in line
 804 with the manufacturer’s technical specification for output swing of $\pm 3 \text{ V}$. Figure 19b shows the same
 805 data as in Fig. 19a, but as function of the charge which arrives at the input of the respective pre-amplifier.
 806 The charge is calculated using V_{input} and the circuit elements shown in Fig. 6. The slope of the anode
 807 2 data before saturation in the plot gives the pre-amplifier gain ($G_{\text{preamp}}^{\text{CR-112}} = 11.7 \pm 0.6 \text{ mV pC}^{-1}$)
 808 multiplied by f^{a2} , which describes signal attenuation and losses in the circuit (cf. Eq. (7)). Fitting of
 809 a polynomial of order one to the data points, corresponding to the anode 2 line in Fig. 19a, yields
 810 $f^{a2} \cdot G_{\text{preamp}}^{\text{CR-112}} = 9.8 \pm 0.1 \text{ mV pC}^{-1}$, the corresponding value for f^{a2} is shown in Tab. 5.

811 For anode 3, however, three regions can be identified in Fig. 19a. There are two regions of distinct
 812 linear increase but with different gradients. The first region – up to a V_{input} of 150 mV – ends at the
 813 point when the anode 2 pre-amplifier saturates. From this point onwards two decay constants are
 814 observed in anode 3 waveforms similar to what is shown in Fig. 18. In the second region the rise is
 815 still linear, but with a different slope than in the first region and the third region covers the saturation
 816 of the anode 3 pre-amplifier. When the anode 2 pre-amplifier saturates, the AC signal current can no
 817 longer simply flow through its input and feedback capacitor and the signal sharing is modified. This
 818 feedback is then seen in the detector as more charge being measured by the anode 3 pre-amplifier
 819 than expected. It has been confirmed that this behaviour is indeed due to the anode 2 pre-amplifier
 820 saturating. Removing this pre-amplifier from the circuit results in anode 3 signals with only one
 821 decay constant and no change in gradient – similar to what is shown for anode 2 in Fig. 19a. A fit of
 822 a polynomial of order one yields $f^{a3} \cdot G_{\text{preamp}}^{\text{CR-112}} = 5.18 \pm 0.07 \text{ mV pC}^{-1}$ for anode 3 before the anode
 823 2 saturation and $f_{\text{post}}^{a3} \cdot G_{\text{preamp}}^{\text{CR-112}} = 8.3 \pm 0.4 \text{ mV pC}^{-1}$ after the saturation. Table 5 shows the circuit
 824 response f obtained by comparing the measurements of $f \cdot G_{\text{preamp}}$ to the bare $G_{\text{preamp}}^{\text{CR-112}}$ measurements
 825 at the beginning of this section.



(a)



(b)

Figure 19. Peak height ($V_{\text{output}}^{\text{amp}}$) measured by the anode 2 and anode 3 readout channel (with pre-amplifier) for test pulses injected into the amplification region via the anode 1 mesh. Both plots show the same data with different units on the horizontal axis: (a) $V_{\text{output}}^{\text{amp}}$ as function of input test pulses signal height (V_{input}) and (b) as a function of the charge seen at the pre-amplifier input. One polynomial of order ($P1$) one is fitted to the anode 2 (blue) measurement and two separate $P1$ s are fitted to the different regions on anode 3. One in the pre-saturation region of the anode 2 pre-amplifier (red) and one in the post-saturation region of anode 2 pre-amplifier (orange).

Anode	$f \cdot G_{\text{preamp}}$ [mV/pC]	Modification factor f
anode 2	9.8 ± 0.1	0.754 ± 0.007
anode 3 Pre-saturation	5.18 ± 0.07	0.398 ± 0.005
anode 3 Post-saturation	8.3 ± 0.4	0.64 ± 0.03

Table 5. Using the measured pre-amplifier without the circuit response ($C_{\text{preamp}}^{\text{CR}-112} = 11.7 \pm 0.6$ mVpC⁻¹) and the measurements of the pre-amplifiers connected to the detector $f \cdot G_{\text{preamp}}$, the circuit response modification-factor f is determined [29].

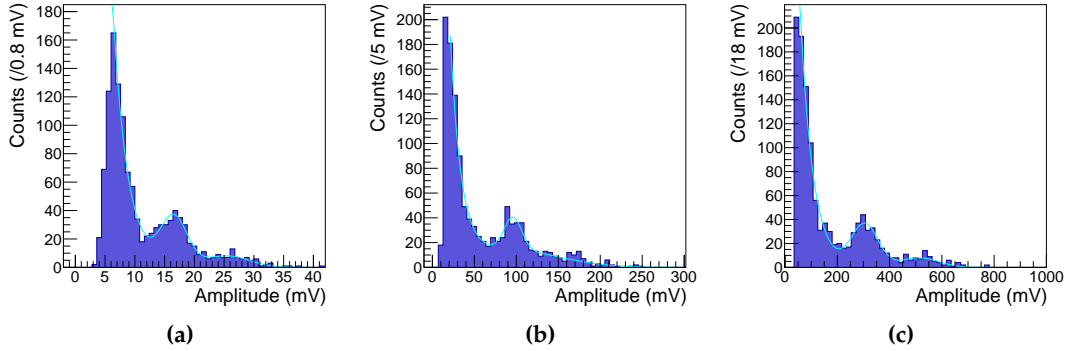


Figure 20. Waveform amplitude spectra for anodes (a) 1, (b) 2, and (c) 3. On the vertical axis counts are shown, normalised to the time of one CCD exposure, *i.e.* 2 s. The spectra are fitted with an exponential plus two Gaussian functions. Amplitude spectra shown are summed data over 15 consecutive runs taken at the same voltage settings, $V_{a1} = 1200$ V, $V_{a2} = 2400$ V, $V_{a3} = 3600$ V, $V_c = -6000$ V.

826 Finding $f = 1$ would imply that there are no signal losses or attenuation effects in the circuit. The f
827 values measured here show a substantial attenuation which can be corrected for since f is constant as
828 a function of amplitude. These losses may occur through the resistive elements shown in Fig. 6. The
829 change in f on anode 3 when the anode 2 pre-amplifier is saturated makes this correction slightly more
830 complicated. The capacitances of the amplification region and the available pulse generator did not
831 allow to drive the anode 3 pre-amplifier into saturation to examine whether a similar feed-back occurs
832 on anode 2. In general, events with either pre-amplifier being saturated occur only rarely, as do events
833 where the signal amplitude on anode 2 is higher than on anode 3 due to the way the amplification
834 region is biased.

835 6.3.2. Charge gain of the amplification region

836 This section discusses the analysis of charge waveform data taken simultaneously as the CCD
837 frames used for the light analysis described in Sec. 5.4. All data was taken in the same TPC fill of pure
838 argon at 3 bar absolute pressure. The three voltage schemes – A, B, and C – are described in detail in
839 the previous section.

840 Determining the Am-241 alpha decay peak amplitude

841 After data cleaning (Sec. 6.2) and taking into account the calibration discussed in Sec. 6.3.1 we
842 create amplitude spectra for each anode per voltage setting as shown in Fig. 20. The number of
843 entries in the amplitude spectra for each voltage configuration varies between 100 and 2500, with an
844 average of 910 entries per configuration. This variation is caused by the fact that at higher voltage
845 settings a greater number of waveforms are recorded and survive the cleaning cuts. From the results
846 presented in Sec. 5.4 (and Sec. 5.3), we are confident that we should see the α particles from the ²⁴¹Am
847 decay in the waveform amplitude spectra. Whilst the qualitative example spectrum in Fig. 8 does
848 neither account for the gas gain and the electronic noise, the measured amplitude spectra should

849 show some resemblance to this simulation. The measured amplitude spectra (Fig. 20) appear as an
 850 exponentially falling background, with a clear peak. This peak corresponds to the deposit of the
 851 ~ 4.5 MeV α particles from the ^{241}Am decay. The exponential background is a mix of the expected
 852 cosmic radiation background, of the ^{241}Am x-ray signals and noise triggers. The amplitude spectra are
 853 fitted with the function

$$s(\text{amplitude}) = \exp\{p_0 + p_1 \cdot \text{amplitude}\} + p_2 \cdot \exp\left\{-0.5 \cdot \left(\frac{\text{amplitude} - p_3}{p_4}\right)^2\right\} + p_5 \cdot \exp\left\{-0.5 \cdot \left(\frac{\text{amplitude} - p_6}{p_7}\right)^2\right\}, \quad (9)$$

854 where the first term is an exponential function to fit the noise, and x-ray and γ -ray background, and
 855 the second term is a Gaussian function to fit the α -peak. The third term is a second Gaussian function
 856 which fits the higher amplitude entries of the spectra, where the spectra are shaped by cosmic muons.
 857 Examples of these fits are shown in Fig. 20.

858 The mean of the Gaussian fitting the α -peak from the ^{241}Am decay, p_3 , is extracted and taken as a
 859 measure for the mean energy deposit of the α particles. In Fig. 21 the α -peak position is plotted against
 860 the varied voltage in the respective voltage scheme. The peak position uncertainty shown in the plots
 861 are the fit uncertainties on the mean of the Gaussian, scaled by the χ^2/N_{dof} of the fit, for fits where
 862 $\chi^2/N_{\text{dof}} > 1$.

863 For Scheme A the peak position is plotted against the voltage of anode 1 (Fig. 21, first row), for
 864 Scheme B the peak position is plotted against the potential difference between anodes 2 and 3 (Fig. 21,
 865 second row), and for Scheme C the peak position is plotted against the potential difference between
 866 anodes 1 and 2 (Fig. 21, third row).

867 Gas gain against voltage for the three voltage schemes

868 Before calculating the gas gain for the three voltage schemes A, B and C from the values in the
 869 amplitude spectra, gas quality degradation needs to be considered. Degrading gas quality can have a
 870 significant effect on the gain measurements, and so we took data at identical gas, pressure and bias
 871 voltage settings every 24 hours to obtain calibration correction as the data used in this analysis was
 872 taken over three days.

873 We reconstruct the peak position in the amplitude spectra of these calibration runs. After the gas quality
 874 calibration is fit to these data points vs. the measurement time. The correction function is $y(\text{time}) = m \cdot$
 875 $\text{time} + b$, where the values of (m, b) are $(0.8 \pm 0.2 \text{ mV/day}, -1 \pm 5 \text{ mV})$, $(11 \pm 2 \text{ mV/day}, -135 \pm 42 \text{ mV})$
 876 and $(27 \pm 7 \text{ mV/day}, -277 \pm 141 \text{ mV})$ for anode 1, anode 2, and anode 3 spectra respectively, and the
 877 calibration is normalized such that the non-calibrated data and the calibrated data have the same value
 878 at the beginning of Scheme C. We observe a drift in the peak position as can be seen from the (m, b)
 879 pairs, however, the drift is such that no change could be observed when examining the amplitude
 880 spectra for each run in a voltage setting individually.

881 A systematic uncertainty contribution is assessed to account for this effect, represented by the dotted
 882 error bars in Fig. 21. This contribution takes the expected peak position shift over the measurement
 883 time in each voltage scheme into account and is calculated as the standard deviation of the measured
 884 peak positions with respect to the peak position after correction.

885 Equation (7) allows now to calculate the gas amplification factor of the amplification region, G_{amp} ,
 886 using

$$G_{\text{amp}} = \frac{A}{f \cdot G_{\text{preamp}} \cdot Q_e} \quad \text{where} \quad (10)$$

$$Q_e = \frac{\langle \varepsilon_\alpha \rangle}{W} \cdot 1.6022 \times 10^{-19} \text{ C} \quad . \quad (11)$$

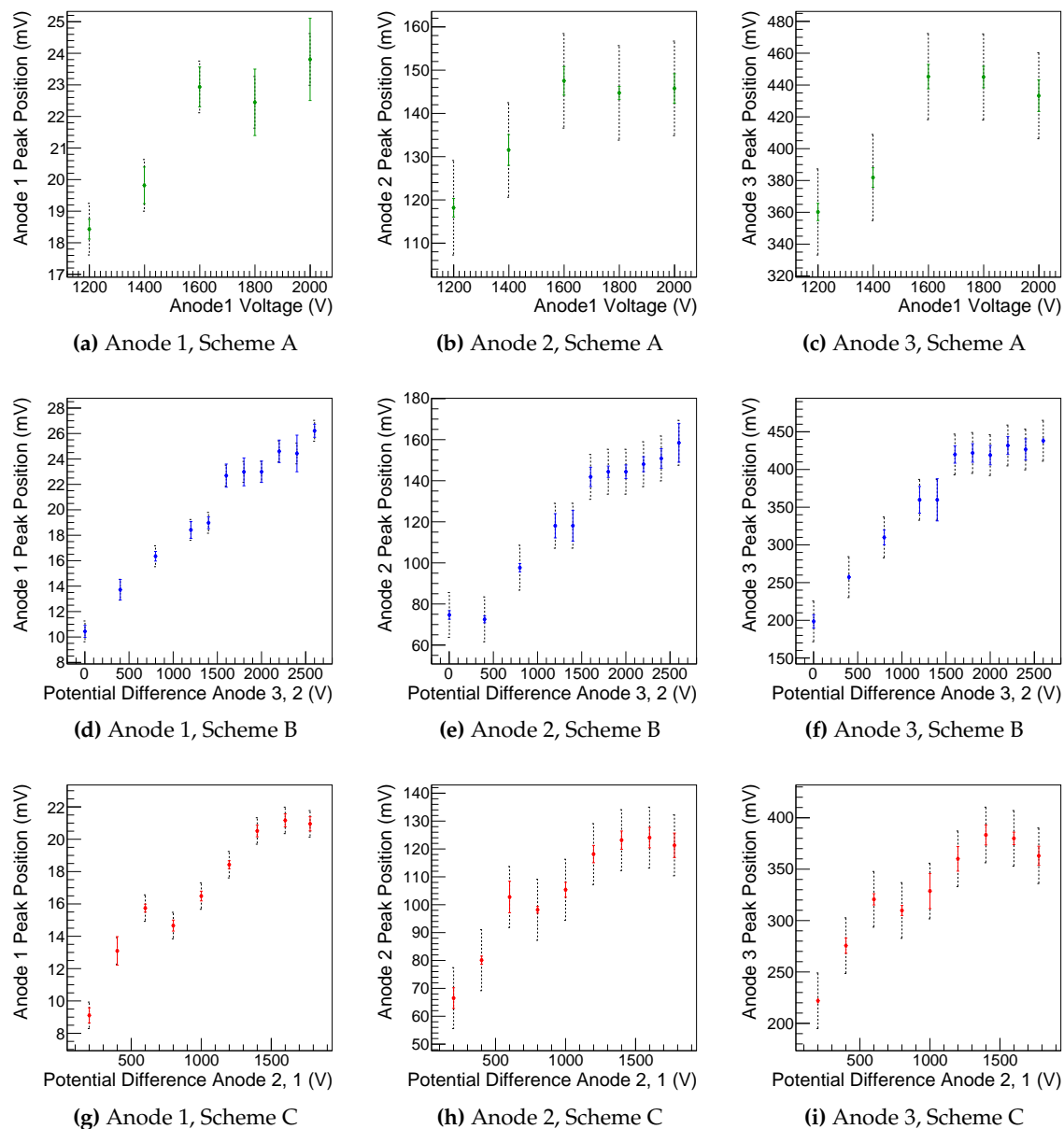


Figure 21. Plots of the position of the α -peak in the respective amplitude spectra. In the first row ((a), (b), and (c)) the peak position is plotted vs anode 1 voltage (Scheme A). During Scheme A, the voltages of all three anodes are increased in steps of 200 V while the potential difference between anodes is kept constant. In the second row (Scheme B: (d), (e), and (f)) the peak position is plotted vs the potential difference between anodes 2 and 3 (ΔV_{a23}). During the measurement V_{a1} , V_{a2} and ΔV_{a12} are kept constant. Third row (Scheme C: (g), (h), and (i)): Peak position vs the potential difference between anodes 1 and 2 (V_{a12}) while V_{a1} and ΔV_{a23} are kept constant. All measurements have been made in the same gas fill of 3 bar absolute of pure argon.

Scheme	Voltage setting (A1 / A2 / A3) [V]		Gas gain at anode 3 at voltage setting	
	Lowest	Highest	at lowest setting	at highest setting
A	1200 / 2400 / 3600	2000 / 3200 / 4400	$(2.61 \pm 0.20) \times 10^3$	$(3.14 \pm 0.20) \times 10^3$
B	1200 / 2400 / 2400	1200 / 3400 / 5000	$(1.44 \pm 0.20) \times 10^3$	$(3.18 \pm 0.20) \times 10^3$
C	1200 / 1400 / 2600	1200 / 3000 / 4200	$(1.61 \pm 0.20) \times 10^3$	$(2.63 \pm 0.20) \times 10^3$

Table 6. The charge gain measured at the highest at lowest voltage settings of each voltage scheme.

887 We calculate G_{amp} for the amplitude spectra measured at each mesh. In the calculation we use the
 888 best-fit peak position of the α -peak in the amplitude spectra to be A , corrected by the calibration
 889 procedure described above. Figure 22 shows the gas gain at each anode plotted against the respective
 890 voltage in the three voltage schemes. The goal of this analysis is to determine the dependence of the
 891 gain on the absolute voltages of the anodes (V_{a1} , V_{a2} , and V_{a3}) and on the potential differences between
 892 the anodes (ΔV_{a12} and ΔV_{a23}). The results of the charge gain measurement for schemes A, B and C
 893 are shown in Fig. 22 in the first, second and third row, respectively, and the gas gains measured at the
 894 highest and lowest voltage settings for each scheme are presented in Tab. 6. The voltage range covered
 895 during the three schemes has been optimised for the light analysis, to the end that i) all voltage settings
 896 of the three schemes could be taken in one gas fill without the degradation of the gas fill, ii) to avoid to
 897 reach a voltage regime where sparking occurs, and iii) to have sufficient overlap between the three
 898 voltage schemes. As a result of this our study of the charge gain of the amplification region covers
 899 only a small gain range (Tab. 6 and Fig. 22).

900 For all three voltage schemes the measured gas gain increases from anode 1, to anode 2, to anode 3, as
 901 is expected from a cascade of amplification stages. The gas amplification factor in Scheme C is overall
 902 the lowest. Examining the multiplication factor between different meshes we find $G_{\text{amp}}^{\text{mesh2}} \sim 8 \cdot G_{\text{amp}}^{\text{mesh1}}$
 903 ($G_{\text{amp}}^{\text{mesh2}} \sim 6.5 \cdot G_{\text{amp}}^{\text{mesh1}}$) and $G_{\text{amp}}^{\text{mesh3}} \sim 5.5 \cdot G_{\text{amp}}^{\text{mesh2}}$ ($G_{\text{amp}}^{\text{mesh3}} \sim 6 \cdot G_{\text{amp}}^{\text{mesh2}}$) in scheme A and Scheme B
 904 (Scheme C). The highest contribution to the combined gas gain $G_{\text{amp}}^{\text{mesh1}} \cdot G_{\text{amp}}^{\text{mesh2}} \cdot G_{\text{amp}}^{\text{mesh3}}$ is thus the
 905 contribution of the anode 1 mesh. The dependence of the gain on the various voltages shows a similar
 906 functional shape as the light gain reported in Sec. 5.4.2, Fig. 15. Due to relatively large uncertainties,
 907 the results in Scheme A are consistent with either a slight dependence or no dependence of the gain
 908 on the absolute voltages of the anodes while ΔV_{a12} and ΔV_{a23} are fixed at 1200 V and are therefore
 909 consistent with the conclusions of the light gain analysis. The results of schemes B and C are consistent
 910 with a positive correlation of gain on ΔV_{a23} and ΔV_{a12} , this is again consistent with the conclusions
 911 drawn from the light gain analysis. The results of the charge gain analysis supports the conclusions
 912 of the light gain analysis, that the amplification is primarily driven by the electric field between the
 913 anodes.

914 7. Combined Optical and Charge Readout Analysis

915 In this section we present the results of the combined optical and charge gain analysis. The optical
 916 and charge gain analyses described in Sec. 5 and Sec. 6 were performed on data taken simultaneously
 917 with both readout systems. We investigate the correlation between optical gain and charge gain in
 918 Fig. 15 and Fig. 22. Plots of the optical gain against the charge gain for Schemes A, B and C are shown
 919 in Fig. 23. Figure 24 shows the ratio of the charge gain to the measured light intensity in ADU as a
 920 function of the relevant voltage in the respective voltage scheme. The larger of the two charge gain
 921 error bars (shown dotted in Fig. 23) has been propagated through to produce the error bars seen in
 922 Fig. 24.

923 To measure the correlation factor between the two gain measurements we use the Pearson
 924 correlation coefficient, which takes values between -1 and 1 for fully negative and positive correlated
 925 data. The coefficient is zero for uncorrelated data. In order to take the uncertainties of our
 926 measurements into account we take every measured value as the centre of a normal distribution
 927 and its uncertainty as the distribution's standard deviation. From these distributions a 1000 random
 928 data series are drawn for each voltage scheme with the same number of points as in the original data

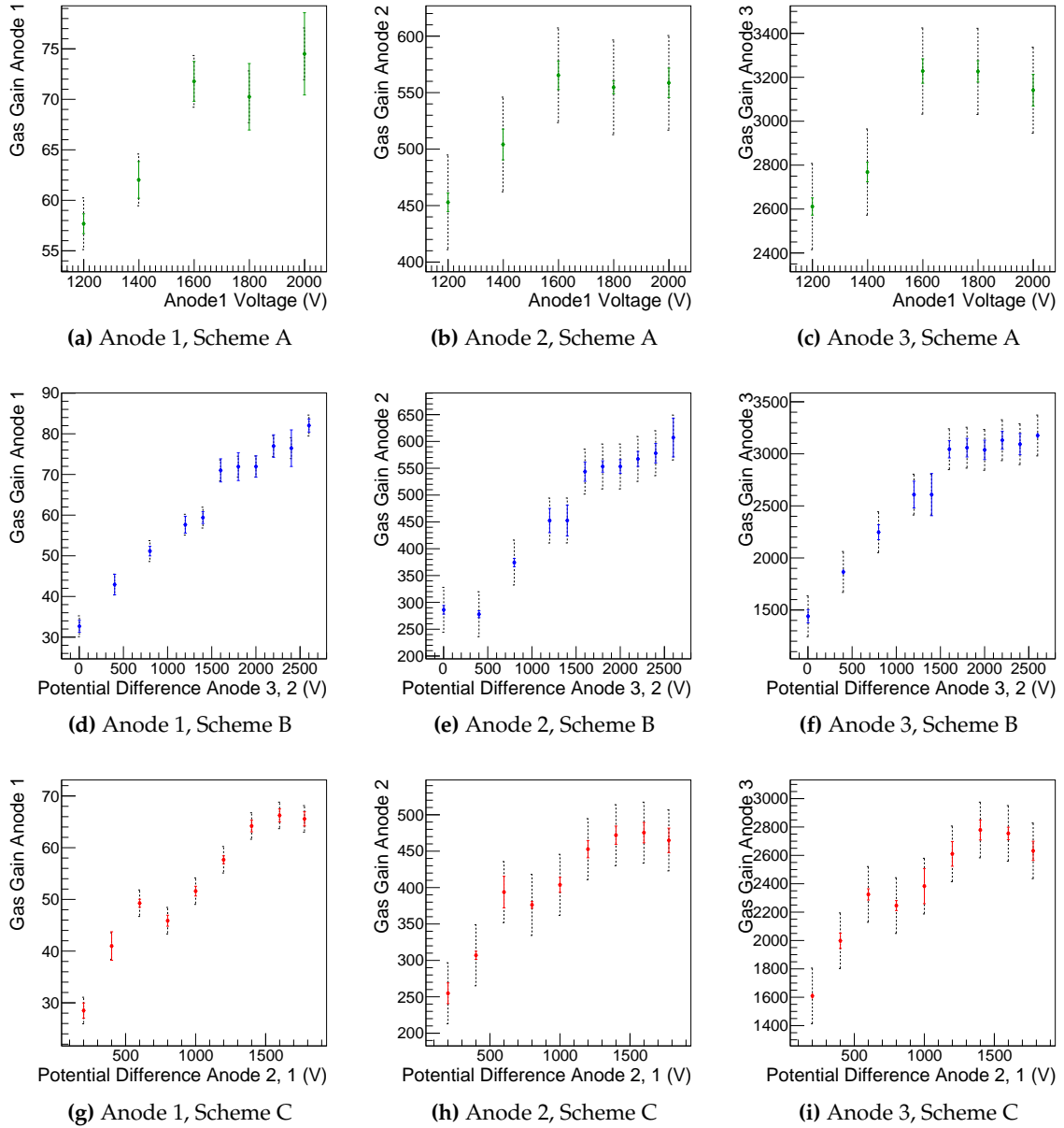


Figure 22. Plots of the calculated gas gain vs either anode voltage or inter-anode voltage difference. The gain is calculated from the data shown in the respective plot in Fig. 21. First row ((a), (b), and (c)): Scheme A, gain vs anode 1 voltage (V_{a1}), V_{a1} , V_{a2} and V_{a3} are increased by the same amount whilst $\Delta V_{a12} = \Delta V_{a23} = 1200$ V. Second row ((d), (e), and (f)): Scheme B, gain vs the voltage difference between anode 2 and 3 (ΔV_{a23}), V_{a3} and ΔV_{a23} are increased whilst $V_{a1} = 1200$ V and $V_{a2} = 2400$ V. Third row ((g), (h), and (i)): Scheme C, gain vs the anode 1 to anode 2 voltage differences (ΔV_{a12}), V_{a2} , ΔV_{a12} and V_{a3} are increased whilst keeping V_{a1} and ΔV_{a23} constant. All data has been taken in the same gas fill of 3 bar absolute of pure argon.

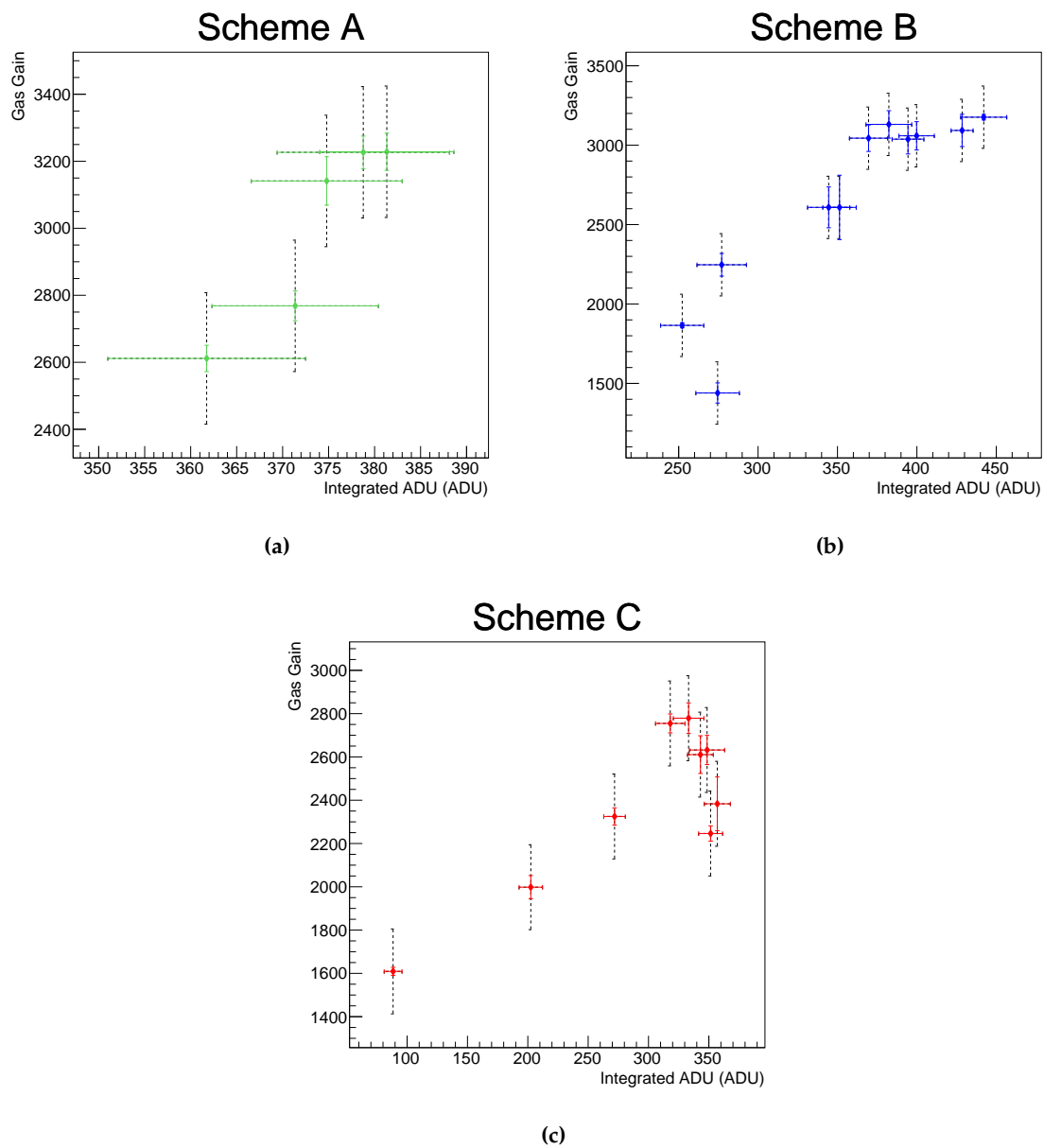


Figure 23. Measured light intensity (Integrated ADU) (Fig. 15) plotted against the gas gain measured in the charge readout on anode 3 (Fig. 22, right column) for Schemes A, B and C.

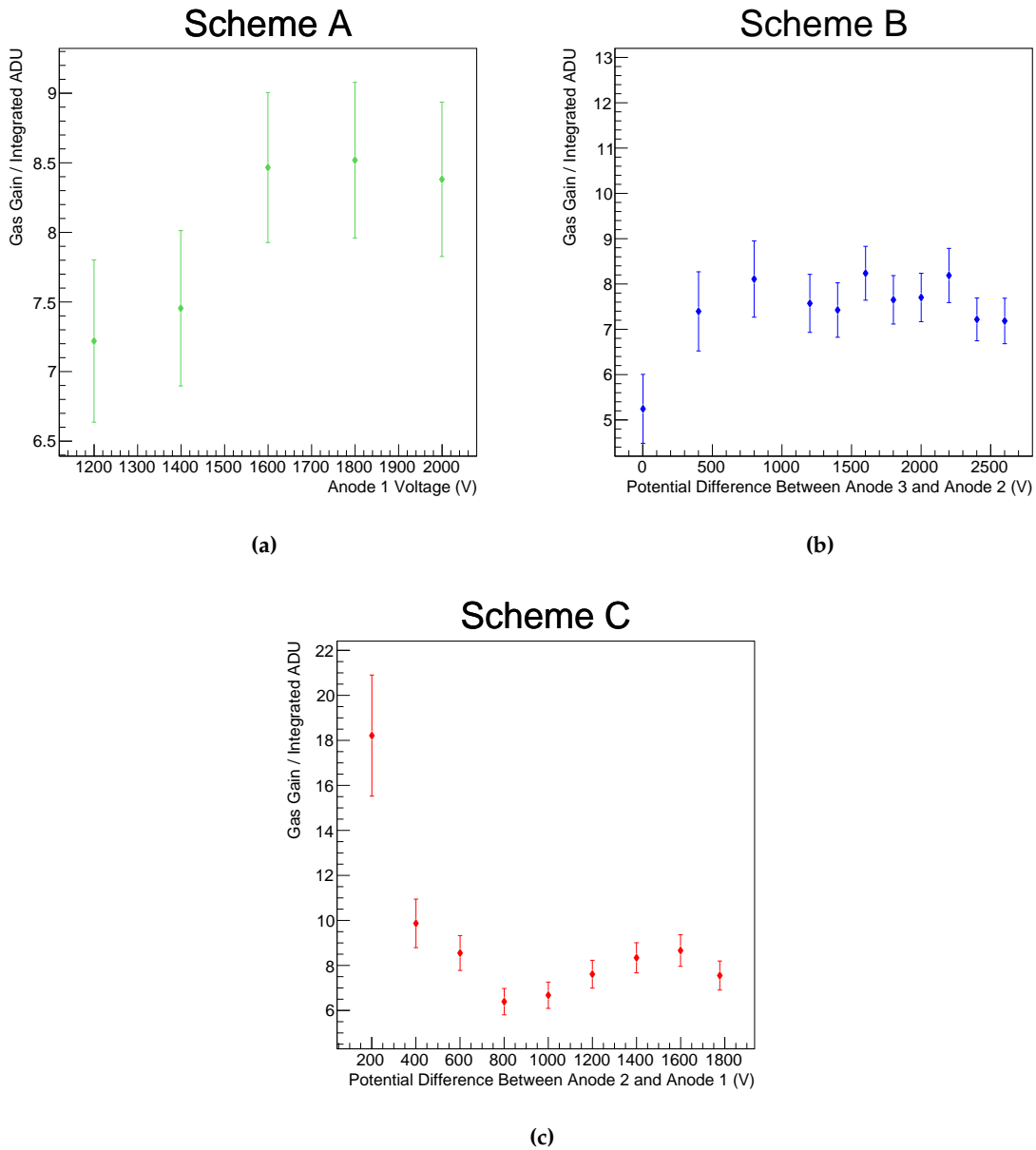


Figure 24. Ratio of gas gain measured in the amplification region at anode 3 (Fig. 22, right column) to the measured intensity (integrated ADU) (Fig. 15) vs (a) anode 1 voltage (V_{a1}) where the voltage differences between the meshes is always $\Delta V_{a12} = \Delta V_{a23} = 1200$ V (b) potential difference between anode 2 and anode 3 (V_{a23}) while the anode 1 and 2 voltages are kept constant (c) potential difference between anodes 1 and 2 (ΔV_{a12}) while V_{a1} is kept constant and ΔV_{a23} is maintained at 1200 V

929 series in Fig. 24a, Fig. 24b and Fig. 24c and the correlation factor is calculated for each of them. The
930 correlation factors quoted in the following are the mean of these 1000 correlation factors and their
931 standard deviation.

932 Both the optical and charge analysis found Scheme A to be consistent with no change in gain.
933 The figures in this section show continued support for this case as expected. The correlation factor of
934 the data sample in Fig. 23a is 0.50 ± 0.37 . Figure 23b and Fig. 23c have a positive correlation between
935 optical and charge gain in Schemes B and C of 0.85 ± 0.06 and 0.75 ± 0.11 . Measuring a correlation
936 between the electron and the photon yield in the amplification region suggests that the measured light
937 is produced within the avalanches and thus the light yield increases with the charge gain. In Scheme C,
938 we see a defined saturation of the optical gain above $\Delta V_{a12} = 800$ V (Fig. 15c). This effect is not clearly
939 visible in the charge gain analysis (Fig. 22i). However, given the size of the gas gain error bars it is not
940 possible to confidently exclude this as a possibility.

941 Figure 24 shows a largely consistent ratio of gas gain to the measured light gain in integrated
942 ADU of around 8 for all schemes. The only deviation from this ratio occurs at the lowest voltage
943 settings for Schemes B and C. In Sec. 5.4.3 we found that there are $(2.2 \pm 0.5) \times 10^{-3}$ photons in the
944 amplification region per primary electron in the drift volume, when analysing the voltage setting with
945 the highest light yield. The authors of [20] examine pure argon at a pressure of 3 bar absolute, too.
946 For this gas they measure, albeit with a much smaller detector and a two mesh amplification region
947 with 4 mm distance, a maximal value of ~ 0.5 photons per primary electron in the drift volume. This is
948 two orders of magnitude higher than the value we observe. Furthermore, they observe this photon
949 yield at a charge gain of about 10 while their measured light gain as function of charge gain saturates
950 somewhere in-between charge gains of 5 and 10. In [20] the measurement is performed with a x-ray
951 tube as radiation source and a photo-diode mounted close to the amplification region. This set-up
952 allows the authors to operate in a low charge gain regime, where the cross-section for excitations can
953 be higher than at larger charge gains where the ionisation cross-section dominates.
954 To improve the concept of an optical HPTPC with a mesh based amplification region it could be
955 considered to have an amplification stage followed by a region of lower field in which the amplified
956 electrons predominately excite gas atoms or molecules. The difficulty with such a combination of
957 amplification and scintillation regions is that the electron transmissions between two meshes depends
958 on the ratio of the fields on either side – therefore only a fraction of the electrons from the high-field
959 amplification gap(s) will reach the low-field scintillation gap.

960 8. Summary

961 In order to reduce neutrino interaction related systematic uncertainties in future neutrino
962 oscillation experiments, a key measurement is proton-nucleus scattering. Hadronic interactions
963 as particles produced in neutrino interactions exit the nucleus and obfuscate the secondary particle
964 multiplicity and kinematics, causing event migrations between data samples and introducing biases in
965 neutrino event reconstruction. Measurements of protons interacting with nuclei can constrain these
966 hadronic interactions and thereby reduce these biases. A HPTPC prototype detector with a three mesh
967 amplification region has been constructed and operated at RHUL and CERN as a first step in the
968 development of a HPTPC capable of performing these measurements.

969 In this work, for the first time, we demonstrate the successful combined optical and charge readout of
970 a hybrid high pressure gaseous TPC with an active volume of ~ 0.5 m³. The optical readout utilises
971 CCD cameras, most sensitive in the visible part of the wavelength spectrum. Using cameras with an
972 increased range of sensitivity to the VUV or wavelength shifting filters could be beneficial in future
973 research. In a series of pilot measurements we identified pure argon at an absolute pressure of 3 bar as
974 the gas best suited to perform in depth tests of the optical readout performance with a high pressure
975 gas. Our measurements were done using the α particles emitted by an Am²⁴¹ source. When using
976 the HPTPC with argon at 3 bar we were not able to image tracks on an event by event basis with the
977 optical readout. This may be due to the large diffusion in pure argon. Integrating over many exposures

978 we measure an increasing light yield when increasing the electric field between mesh 2 and mesh 3
979 (E_{a23}), where the mesh number increases for anodes further away from drift region. An increase in
980 light yield is also measured when increasing the field between mesh 1 and mesh 2 (E_{a12}). In this case
981 the light yield reaches a plateau when $E_{a12} \sim E_{a23}$. At the maximum light yield measured, we find
982 that there are $(2.2 \pm 0.5) \times 10^{-3}$ photons in the amplification region per primary electron in the drift
983 volume.

984 The analysis of the charge signals reveals that light gain and charge gain are correlated and that the gas
985 gain at the voltage settings of the maximal light yield is 3000. The first mesh in the cascade contributes
986 the largest fraction of the amplification stages gain of ~ 70 whilst the following meshes contribute
987 another factor of about 8 and 5.5, respectively.

988 **Author Contributions:** Conceptualization, Anastasia Basharina-Freshville, Steven Boyd, Dominic Brailsford,
989 Linda Cremonesi, Patrick Dunne, Jennifer Haigh, Asher Kaboth, Jocelyn Monroe, Ryan Nichol, Jaroslaw Nowak,
990 Ruben Saakyan, Nicola Serra, Yuri Shitov and Morgan Wascko;

991 Data curation, Alexander Deisting, Abigail Waldron, Edward Atkin, Dominic Brailsford, Zachary
992 Chen-Wishart, Linda Cremonesi, Adriana Dias, Patrick Dunne, Jennifer Haigh, Philip Hamacher-Baumann,
993 Sebastian Jones, Asher Kaboth, Alexander Korzenev, Maria Mironova, Jocelyn Monroe, Ryan Nichol, Toby
994 Nonnenmacher, Jaroslaw Nowak, William Parker, Harrison Ritchie-Yates, Stefan Roth, Adam Tarrant, Melissa
995 Uchida, Sammy Valder, Mark Ward and Morgan Wascko;

996 Formal analysis, Alexander Deisting, Abigail Waldron, Edward Atkin, Dominic Brailsford, Zachary
997 Chen-Wishart, Adriana Dias, Patrick Dunne, Jennifer Haigh, Philip Hamacher-Baumann, Sebastian Jones, Maria
998 Mironova, Toby Nonnenmacher, William Parker, Harrison Ritchie-Yates, Adam Tarrant and Mark Ward;

999 Funding acquisition, Gary Barker, Anastasia Basharina-Freshville, Steven Boyd, Asher Kaboth, Jocelyn
1000 Monroe, Ryan Nichol, Jaroslaw Nowak, Stefan Roth, Ruben Saakyan and Morgan Wascko;

1001 Investigation, Alexander Deisting, Abigail Waldron, Edward Atkin, Gary Barker, Anastasia
1002 Basharina-Freshville, Christopher Betancourt, Dominic Brailsford, Zachary Chen-Wishart, Linda Cremonesi,
1003 Adriana Dias, Patrick Dunne, Jennifer Haigh, Philip Hamacher-Baumann, Sebastian Jones, Asher Kaboth,
1004 Alexander Korzenev, William Ma, Philippe Mermod, Maria Mironova, Jocelyn Monroe, Ryan Nichol, Toby
1005 Nonnenmacher, Jaroslaw Nowak, William Parker, Harrison Ritchie-Yates, Stefan Roth, Ruben Saakyan, Nicola
1006 Serra, Yuri Shitov, Jochen Steinmann, Adam Tarrant, Melissa Uchida, Sammy Valder, Mark Ward and Morgan
1007 Wascko;

1008 Methodology, Alexander Deisting, Abigail Waldron, Gary Barker, Anastasia Basharina-Freshville,
1009 Christopher Betancourt, Steven Boyd, Dominic Brailsford, Zachary Chen-Wishart, Linda Cremonesi, Adriana Dias,
1010 Patrick Dunne, Jennifer Haigh, Philip Hamacher-Baumann, Sebastian Jones, Asher Kaboth, Alexander Korzenev,
1011 William Ma, Philippe Mermod, Maria Mironova, Jocelyn Monroe, Ryan Nichol, Toby Nonnenmacher, Jaroslaw
1012 Nowak, William Parker, Harrison Ritchie-Yates, Stefan Roth, Ruben Saakyan, Nicola Serra, Yuri Shitov, Jochen
1013 Steinmann, Adam Tarrant, Melissa Uchida, Sammy Valder, Mark Ward and Morgan Wascko;

1014 Project administration, Alexander Deisting, Gary Barker, Steven Boyd, Linda Cremonesi, Asher Kaboth,
1015 Jocelyn Monroe, Ryan Nichol, Jaroslaw Nowak and Morgan Wascko;

1016 Resources, Steven Boyd, Dominic Brailsford, Linda Cremonesi, Asher Kaboth, Jocelyn Monroe, Ryan Nichol,
1017 Jaroslaw Nowak, Stefan Roth and Morgan Wascko;

1018 Software, Alexander Deisting, Abigail Waldron, Edward Atkin, Patrick Dunne, Jennifer Haigh, Philip
1019 Hamacher-Baumann, Sebastian Jones, Toby Nonnenmacher, William Parker, Harrison Ritchie-Yates, Adam Tarrant
1020 and Sammy Valder;

1021 Supervision, Alexander Deisting, Abigail Waldron, Gary Barker, Anastasia Basharina-Freshville, Steven
1022 Boyd, Linda Cremonesi, Patrick Dunne, Asher Kaboth, Jocelyn Monroe, Ryan Nichol, Jaroslaw Nowak, Ruben
1023 Saakyan and Morgan Wascko;

1024 Validation, Alexander Deisting, Abigail Waldron, Edward Atkin, Dominic Brailsford, Zachary Chen-Wishart,
1025 Linda Cremonesi, Patrick Dunne, Sebastian Jones, Asher Kaboth, Maria Mironova, Jocelyn Monroe, Ryan Nichol,
1026 Toby Nonnenmacher, Harrison Ritchie-Yates and Adam Tarrant;

1027 Visualization, Alexander Deisting, Abigail Waldron, Edward Atkin, Zachary Chen-Wishart, Adriana Dias,
1028 Patrick Dunne, Philip Hamacher-Baumann, William Parker and Harrison Ritchie-Yates;

1029 Writing – original draft, Alexander Deisting, Abigail Waldron, Zachary Chen-Wishart, Patrick Dunne, Asher
1030 Kaboth, Jocelyn Monroe, William Parker, Harrison Ritchie-Yates, Adam Tarrant and Morgan Wascko;

1031 Writing – review & editing, Alexander Deisting, Abigail Waldron, Edward Atkin, Dominic Brailsford,
1032 Zachary Chen-Wishart, Linda Cremonesi, Adriana Dias, Patrick Dunne, Philip Hamacher-Baumann, Asher
1033 Kaboth, Jocelyn Monroe, Jaroslaw Nowak, Harrison Ritchie-Yates and Morgan Wascko.

1034 **Funding:** This research was funded in part by Science and Technology Facilities Council grant number
1035 ST/N003233/.

1036 **Acknowledgments:** We wish to acknowledge support for summer students from the Ogden Trust and St. Andrews
1037 University, and outstanding support during the beam test from Johannes Bernhard of CERN as well as Johan
1038 Borg, Rebecca Conybeare, Nicole Cullen, Kate Gould, Maria Khaleeq, Veera Mikola, Duncan Parker, Christopher
1039 Thorpe and Simon Williams.

1040 **Conflicts of Interest:** The authors declare no conflict of interest.

1041 References

1042

- 1043 1. Abe, K.; others. Constraint on the Matter-Antimatter Symmetry-Violating Phase in Neutrino Oscillations.
1044 *Nature* **2020**, *580*, 339–344, [[arXiv:hep-ex/1910.03887](https://arxiv.org/abs/1910.03887)]. doi:10.1038/s41586-020-2177-0.
- 1045 2. Alvarez-Ruso, L.; others. NuSTEC White Paper: Status and challenges of neutrino–nucleus scattering.
1046 *Prog. Part. Nucl. Phys.* **2018**, *100*, 1–68, [[arXiv:hep-ph/1706.03621](https://arxiv.org/abs/1706.03621)]. doi:10.1016/j.ppnp.2018.01.006.
- 1047 3. Hayato, Y. NEUT. *Nucl. Phys. Proc. Suppl.* **2002**, *112*, 171–176. [171(2002)],
1048 doi:10.1016/S0920-5632(02)01759-0.
- 1049 4. Andreopoulos, C.; Barry, C.; Dytman, S.; Gallagher, H.; Golan, T.; Hatcher, R.; Perdue, G.; Yarba, J. The
1050 GENIE Neutrino Monte Carlo Generator: Physics and User Manual **2015**. [[arXiv:hep-ph/1510.05494](https://arxiv.org/abs/1510.05494)].
- 1051 5. Hamilton, P.A. A Study of Neutrino Interactions in Argon Gas. PhD thesis, Imperial College London, 2017.
1052 Phd Thesis.
- 1053 6. MicroBooNE-Collaboration. "Measurement of Reconstructed Charged Particle Multiplicities of Neutrino
1054 Interactions in MicroBooNE". *MICROBOONE PUBLIC NOTE* **2017**, 1024.
- 1055 7. Breskin, A.; others. A Highly Efficient Low Pressure UV Rich Detector With Optical Avalanche Recording.
1056 *Nucl. Instrum. Meth.* **1988**, *A273*, 798–804. [387(1988)], doi:10.1016/0168-9002(88)90099-X.
- 1057 8. Buckland, K.N.; Lehner, M.J.; Masek, G.E.; Mojaver, M. Low pressure gaseous detector for particle dark
1058 matter. *Phys. Rev. Lett.* **1994**, *73*, 1067–1070. doi:10.1103/PhysRevLett.73.1067.
- 1059 9. Fonte, P.; Breskin, A.; Charpak, G.; Dominik, W.; Sauli, F. Beam test of an imaging high-density projection
1060 chamber. *Nuclear Instruments and Methods in Physics Research Section A: Accelerators, Spectrometers, Detectors
1061 and Associated Equipment* **1989**, *283*, 658–664. doi:https://doi.org/10.1016/0168-9002(89)91436-8.
- 1062 10. Dujmic, D.; others. Observation of the 'head-tail' effect in nuclear recoils of low-energy neutrons.
1063 *Nucl. Instrum. Meth.* **2008**, *A584*, 327–333, [[arXiv:physics.ins-det/0708.2370](https://arxiv.org/abs/physics.ins-det/0708.2370)]. [Erratum: *Nucl. Instrum.
1064 Meth.*A592,123(2008)], doi:10.1016/j.nima.2008.04.001, 10.1016/j.nima.2007.10.037.
- 1065 11. Baracchini, E.; Benussi, L.; Bianco, S.; Capoccia, C.; Caponero, M.; Cavoto, G.; Cortez, A.; Costa,
1066 I.; Marco, E.D.; D'Imperio, G.; Dho, G.; Iacoangeli, F.; Maccarrone, G.; Marafini, M.; Mazzitelli, G.;
1067 Messina, A.; Nobrega, R.; Orlandi, A.; Paoletti, E.; Passamonti, L.; Petrucci, F.; Piccolo, D.; Pierluigi, D.;
1068 Pinci, D.; Renga, F.; Rosatelli, F.; Russo, A.; Saviano, G.; Tomassini, S. CYGNO: a gaseous TPC with
1069 optical readout for dark matter directional search. *Journal of Instrumentation* **2020**, *15*, C07036–C07036.
1070 doi:10.1088/1748-0221/15/07/c07036.
- 1071 12. Gai, M.; others. An Optical Readout TPC (O-TPC) for Studies in Nuclear Astrophysics
1072 With Gamma-Ray Beams at HIGS. *JINST* **2010**, *5*, P12004, [[arXiv:physics.ins-det/1101.1940](https://arxiv.org/abs/physics.ins-det/1101.1940)].
1073 doi:10.1088/1748-0221/5/12/P12004.
- 1074 13. Fujiwara, T.; Mitsuya, Y.; Fushie, T.; Murata, K.; Kawamura, A.; Koishikawa, A.; Toyokawa, H.; Takahashi,
1075 H. Gas scintillation glass GEM detector for high-resolution X-ray imaging and CT. *Nuclear Instruments and
1076 Methods in Physics Research Section A: Accelerators, Spectrometers, Detectors and Associated Equipment* **2017**,
1077 *850*, 7–11. doi:https://doi.org/10.1016/j.nima.2017.01.013.
- 1078 14. Klyachko, A.; Friesel, D.; Kline, C.; Liechty, J.; Nichiporov, D.; Solberg, K. Dose Imaging Detectors
1079 for Radiotherapy Based on Gas Electron Multipliers. *Nuclear instruments and methods in physics
1080 research. Section A, Accelerators, spectrometers, detectors and associated equipment* **2011**, *628*, 434–439.
1081 doi:10.1016/j.nima.2010.07.019.
- 1082 15. Brunbauer, F.M.; Lupberger, M.; Oliveri, E.; Resnati, F.; Ropelewski, L.; Strelci, C.; Thuiner, P.; van
1083 Stenis, M. Radiation imaging with optically read out GEM-based detectors. *JINST* **2018**, *13*, T02006.
1084 doi:10.1088/1748-0221/13/02/T02006.
- 1085 16. Leyton, M. Directional dark matter detection with the DMTPC m³ experiment. *J. Phys. Conf. Ser.* **2016**,
1086 *718*, 042035. doi:10.1088/1742-6596/718/4/042035.
- 1087 17. Battat, J.; Irastorza, I.; Aleksandrov, A.; Asada, T.; Baracchini, E.; Billard, J.; Bosson, G.; Bourrion, O.;
1088 Bouvier, J.; Buonaura, A.; Burdge, K.; Cebrián, S.; Colas, P.; Consiglio, L.; Dafni, T.; D'Ambrosio,
1089 N.; Deaconu, C.; Lellis, G.D.; Descombes, T.; Crescenzo, A.D.; Marco, N.D.; Druitt, G.; Eggleston, R.;

- 1090 Ferrer-Ribas, E.; Fusayasu, T.; Galán, J.; Galati, G.; García, J.; Garza, J.; Gentile, V.; Garcia-Sciveres, M.;
1091 Giomataris, Y.; Guerrero, N.; Guillaudin, O.; Guler, A.; Harton, J.; Hashimoto, T.; Hedges, M.; Iguaz,
1092 F.; Ikeda, T.; Jaegle, I.; Kadyk, J.; Katsuragawa, T.; Komura, S.; Kubo, H.; Kuge, K.; Lamblin, J.; Lauria,
1093 A.; Lee, E.; Lewis, P.; Leyton, M.; Loomba, D.; Lopez, J.; Luzón, G.; Mayet, F.; Mirallas, H.; Miuchi, K.;
1094 Mizumoto, T.; Mizumura, Y.; Monacelli, P.; Monroe, J.; Montesi, M.; Naka, T.; Nakamura, K.; Nishimura,
1095 H.; Ochi, A.; Papevangelou, T.; Parker, J.; Phan, N.; Pupilli, F.; Richer, J.; Riffard, Q.; Rosa, G.; Santos,
1096 D.; Sawano, T.; Sekiya, H.; Seong, I.; Snowden-Ifft, D.; Spooner, N.; Sugiyama, A.; Taishaku, R.; Takada,
1097 A.; Takeda, A.; Tanaka, M.; Tanimori, T.; Thorpe, T.; Tioukov, V.; Tomita, H.; Umemoto, A.; Vahsen, S.;
1098 Yamaguchi, Y.; Yoshimoto, M.; Zayas, E. Readout technologies for directional WIMP Dark Matter detection.
1099 *Physics Reports* **2016**, *662*, 1 – 46. Readout technologies for directional WIMP Dark Matter detection,
1100 doi:<https://doi.org/10.1016/j.physrep.2016.10.001>.
- 1101 18. Deaconu, C.; Leyton, M.; Corliss, R.; Druitt, G.; Eggleston, R.; Guerrero, N.; Henderson, S.; Lopez, J.;
1102 Monroe, J.; Fisher, P. Measurement of the directional sensitivity of Dark Matter Time Projection Chamber
1103 detectors. *Phys. Rev.* **2017**, *D95*, 122002, [[arXiv:astro-ph.IM/1705.05965](https://arxiv.org/abs/1705.05965)]. doi:10.1103/PhysRevD.95.122002.
1104 19. Buzulutskov, A.; Bondar, A.; Grebenuk, A. Infrared scintillation yield in gaseous and liquid argon. *EPLA*
1105 **2011**, *94*.
- 1106 20. Fraga, M.M.R.; Bueno, C.C.; Gonçalves, J.A.C.; Farga, F.A.F.; Ferreira Marques, R.; Policarpo, A.J.P.L.
1107 Pressure Dependence of Secondary NIR Scintillation in Ar and Ar-CF₄. *IEEE TRANSACTIONS ON*
1108 *NUCLEAR SCIENCE* **2001**, *48*.
- 1109 21. Lindblom, P.; Solin, O. Atomic near-infrared noble gas scintillations I: Optical spectra. *Nuclear Instruments*
1110 *and Methods in Physics Research Section A: Accelerators, Spectrometers, Detectors and Associated Equipment* **1988**,
1111 *268*, 204 – 208. doi:[https://doi.org/10.1016/0168-9002\(88\)90607-9](https://doi.org/10.1016/0168-9002(88)90607-9).
- 1112 22. Fraga, M.M.; Fetal, S.T.G.; Fraga, F.A.F.; Antunes, E.; Gonçalves, J.; Bueno, C.C.; Ferreira Marques, R.;
1113 Policarpo, A.J.P.L. Study of Scintillation Light from Microstructure Based Detectors. *IEEE TRANSACTIONS*
1114 *ON NUCLEAR SCIENCE* **2000**, *48*.
- 1115 23. Biagi, S. Magboltz 2. *CERN computer newsletter No.2000-001 in section 'Scientific Applications and Software*
1116 *Engineering'* **2000**.
- 1117 24. Ritchie-Yates, H. Commissioning a New Particle Detector Technology: The High Pressure Time Projection
1118 Chamber. PhD thesis, Royal Holloway University of London at Egham (UK), Egham (UK), 2018. Masters
1119 Thesis.
- 1120 25. International Atomic Energy Agency. Nuclear Data Section. 2019. [Online; accessed 13-June-2019].
- 1121 26. Henderson, S.W. An Assessment of the Sensitivity of a Low Pressure Time Projection Chamber to the
1122 Direction of WIMP-Induced Nuclear Recoils. PhD thesis, Massachusetts Institute of Technology, 2006.
1123 Phd Thesis.
- 1124 27. Smirnov, I. Modeling of ionization produced by fast charged particles in gases. *Nuclear Instruments and*
1125 *Methods in Physics Research Section A: Accelerators, Spectrometers, Detectors and Associated Equipment* **2005**,
1126 *554*, 474 – 493. doi:<https://doi.org/10.1016/j.nima.2005.08.064>.
- 1127 28. Baraka, K.; Folkestad, A.; Frolov, E.; Heijhoff, K.; Mott, J.; Pfeiffer, D.; Renner, J.; Schindler, H.; Sheharyar,
1128 A.; Shiell, N.; Veenhof, R.; Zenker, K. Garfield++.
- 1129 29. Tarrant, A. Development of Gas Electron Multipliers (GEMs) for hybrid-readout gaseous Time Projection
1130 Chambers in Future Neutrino Experiments. PhD thesis, Royal Holloway University of London at Egham
1131 (UK), Egham (UK), 2020. Masters Thesis.
- 1132 30. DeLoach, R. A Study of the Feasibility of Applying Capacitive Displacement-measuring Techniques to
1133 Open-mesh Grid Structures. *NASA Technical Note (TN)* **1971**.
- 1134 31. Bergström, K.; Sunner, S. The Relative Permittivity of Argon, Carbon Dioxide, and Hydrogen,
1135 Determined at 10 kHz Using a Transformer Bridge Method. *Physica Scripta* **1976**, *13*, 51–52.
1136 doi:10.1088/0031-8949/13/1/007.